



1 Active tectonic field for CO<sub>2</sub> Storage management: Hontomín onshore  
2 study-case (SPAIN)

3  
4 Raúl Pérez-López<sup>1</sup>, José F. Mediato<sup>1</sup>, Miguel A. Rodríguez-Pascua<sup>1</sup>, Jorge L. Giner-Robles<sup>2</sup>,  
5 Adrià Ramos<sup>1</sup>, Silvia Martín-Velázquez<sup>3</sup>, Roberto Martínez-Orío<sup>1</sup>, Paula Fernández-Canteli<sup>1</sup>

6  
7 1. IGME – Instituto Geológico y Minero de España – Geological Survey of Spain. C/Ríos Rosas 23,  
8 Madrid 28003 – SPAIN. Email: [r.perez@igme.es](mailto:r.perez@igme.es), [jf.mediato@igme.es](mailto:jf.mediato@igme.es), [ma.rodriuez@igme.es](mailto:ma.rodriuez@igme.es),  
9 [ro.martinez@igme.es](mailto:ro.martinez@igme.es), [a.ramos@igme.es](mailto:a.ramos@igme.es); [paula.canteli@igme.es](mailto:paula.canteli@igme.es)  
10 2. Departamento de Geología y Geoquímica. Facultad de Ciencias. Universidad Autónoma de Madrid.  
11 Campus Cantoblanco, Madrid. SPAIN. Email: [jorge.giner@uam.es](mailto:jorge.giner@uam.es)  
12 3. Universidad Rey Juan Carlos. Email: [silvia.martin@urjc.es](mailto:silvia.martin@urjc.es)

13  
14 *Abstract*

15 *One of the concerns of underground CO<sub>2</sub> onshore storage is the triggering of Induced*  
16 *Seismicity and fault reactivation. Hence, a comprehensive analysis of the tectonic*  
17 *parameters involved in the storage rock formation is mandatory for safety management*  
18 *operations. Unquestionably, active faults and seal faults depicting the storage bulk are*  
19 *relevant parameters to be considered. However, there is a lack of analysis of the active*  
20 *tectonic strain field affecting these faults during the CO<sub>2</sub> storage monitoring. The*  
21 *advantage of reconstructing the tectonic field is the possibility to determine the strain*  
22 *trajectories and describing the fault patterns affecting the reservoir rock. In this work,*  
23 *we adapt a methodology of systematic geostructural analysis to the underground CO<sub>2</sub>*  
24 *storage, based on the calculation of the strain field and defined by the strain field from*  
25 *kinematics indicators on the fault planes ( $e_y$  and  $e_x$  for the maximum and minimum*  
26 *horizontal shortening respectively). This methodology is based on a statistical analysis*  
27 *of individual strain tensor solutions obtained from fresh outcrops. Consequently, we*  
28 *have collected 447 fault data in 32 field stations located within a 20 km radius. The*  
29 *understanding of the fault sets role for underground fluid circulation can also be*  
30 *established, helping for further analysis of CO<sub>2</sub> leakage and seepage. We have applied*  
31 *this methodology to Hontomín onshore CO<sub>2</sub> storage facilities (Central Spain). The*



32 *geology of the area and the number of high-quality outcrops made this site as a good*  
33 *candidate for studying the strain field from kinematics fault analysis. The results*  
34 *indicate a strike-slip tectonic regime with the maximum horizontal shortening with*  
35 *N160°E and N50°E trend for the local regime, which activates NE-SW strike-slip faults*  
36 *and NE-SW compressional faults. A regional tectonic field was also recognized with a*  
37 *N-S trend, which activates E-W compressional faults. Monitoring of E-W faults within*  
38 *the reservoir is suggested in addition to the possibility of obtaining focal mechanism*  
39 *solutions for microearthquakes ( $M < 3$ ).*

40

41 Keywords: onshore CO<sub>2</sub> storage, tectonic field, paleostrain analysis, active fault,  
42 Hontomín onshore pilot-plant.

43

#### 44 1. INTRODUCTION

45 Industrial made-man activities generate CO<sub>2</sub> that could change the chemical balance of  
46 the atmosphere and their relationship with the geosphere. Carbon capture and  
47 sequestration (CCS) appears as a good choice to reduce the CO<sub>2</sub> gas emission to the  
48 atmosphere (Christensen, 2004), allowing the industry increasing activity with a low  
49 pollution impact. There is a lot of literature about what must have a site to be a potential  
50 underground storage suitable to CCS (e.g. Chu, 2009; Orr, 2009; Goldberg et al., 2010  
51 among others). The reservoir sealing, the caprock, permeability and porosity, plus  
52 injection pressure and volume injected, are the main considerations to choose one  
53 geological subsurface formation as the CO<sub>2</sub> host-rock. In this frame, the tectonic active  
54 field is considered in two principal ways: (1) to prevent the fault activation and  
55 earthquakes triggering, with the consequence of leakage and seepage, and (2) the long-  
56 term reservoir behavior, understanding as long-term from centennial to millennial time-



57 span. Therefore, what is the long-term behavior of CCS? What do we need to monitor  
58 for a safe CCS management? Winthaegen et al. (2005) suggest three subjects for  
59 monitoring: (a) the atmosphere air quality near the injection facilities, due to the CO<sub>2</sub>  
60 toxicity (values greater than 4%, see Rice, 2003 and Permentier et al., 2017), (b) the  
61 overburden monitoring faults and wells and (c) the sealing of the reservoir. The study of  
62 natural analogues for CCS is a good strategy to estimate the long-term behavior of the  
63 reservoir, considering parameters as the injected CO<sub>2</sub> pressure and volume, plus the  
64 brine mixing with CO<sub>2</sub> (Pearce, 2006). Hence, the prediction of site performance over  
65 long timescales also requires an understanding of CO<sub>2</sub> behavior within the reservoir, the  
66 mechanisms of migration out of the reservoir, and the potential impacts of a leak on the  
67 near surface environment. The assessments of such risks will rely on a combination of  
68 predictive models of CO<sub>2</sub> behavior, including the fluid migration and the long-term  
69 CO<sub>2</sub>-porewater-mineralogical interactions (Pearce, 2006). Once again, the tectonic  
70 active field interacts directly on this assessment. Moreover, the fault reactivation due to  
71 the pore pressure increasing during the injection and storage has also to be considered  
72 (Röhmann et al., 2013). Despite the uplift measure by Röhmann et al. (2013) are  
73 submillimeter (c.a. 0.021 mm) at the end of the injection processes, given the ongoing  
74 occurrence of microearthquakes, long-term monitoring is required. The geomechanical  
75 and geological models predict the reservoir behavior and the caprock sealing properties.  
76 The role of the faults inside these models is crucial for the tectonic long-term behavior  
77 and the reactivation of faults that could trigger earthquakes.

78 Concerning the Induced Seismicity, Wilson et al. (2017) published the Hi-Quake  
79 database, with a classification of all man-made earthquakes according to the literature,  
80 in an online repository (<https://inducedearthquakes.org/>, last access on May, 2019). This  
81 database includes 834 projects with proved Induced Seismicity, where two different



82 cases with earthquakes as large as  $M 1.7$ , detected in swarms about 9,500  
83 microearthquakes, are related to CCS operations. Additionally, Foulger et al. (2018)  
84 pointed out that CCS can trigger earthquakes with magnitudes lesser than  $M 2$ , namely  
85 the cases described in their work are as large as  $M 1.8$ , with the epicenter location 2  
86 km around the facilities. McNamara (2016) described a comprehensive method and  
87 protocol for monitoring CCS reservoir for the assessment and management of Induced  
88 Seismicity. The knowledge of active fault patterns and the stress/strain field could help  
89 on designing monitoring network and identifying those faults capable for triggering  
90 micro-earthquakes ( $M < 2$ ) and/or breaking the sealing for leakage (patterns of open  
91 faults for low-permeability  $\text{CO}_2$  migration).

92 In this work, we propose that the description, the analysis and establishment of the  
93 tectonic strain field have to be mandatory for long-term CCS monitoring and  
94 management, implementing the fault behavior in the geomechanical models. This  
95 analysis does not increase the cost for long-term monitoring, given that they are low-  
96 cost and the results are acquired in a few months. Therefore, we propose a methodology  
97 based on the reconstruction of the strain field from the classical studies in geodynamics  
98 (Angelier, 1979 and 1984; Reches, 1983; Reches, 1987). As a novelty, we introduce the  
99 strain fields (SF) between 20 away from the subsurface reservoir deep geometry. The  
100 knowledge of the strain field at local scale allows to classify the type of faulting and  
101 their role for leakage processes, whilst the regional scale explores the tectonic active  
102 faults which could affect the reservoir. The methodology is rather simple, taking  
103 measures of slickensides and striations on fault planes to establish the orientation of the  
104 maximum horizontal shortening ( $e_y$ ), and the minimum horizontal shortening ( $e_x$ ) for  
105 the strain tensor. The principal advantage of the SF analysis is the direct classification



106 of all the faults involved into the geomechanical model and the prediction of the failure  
107 parameters.

108 The tectonic characterization of the CCS of Hontomín was implemented in the  
109 geological model described by Le Gallo and de Dios (2018). Beyond the use of Induced  
110 Seismicity and potentially active faults, the scope of this method is to propose an initial  
111 protocol to manage underground storage operations.

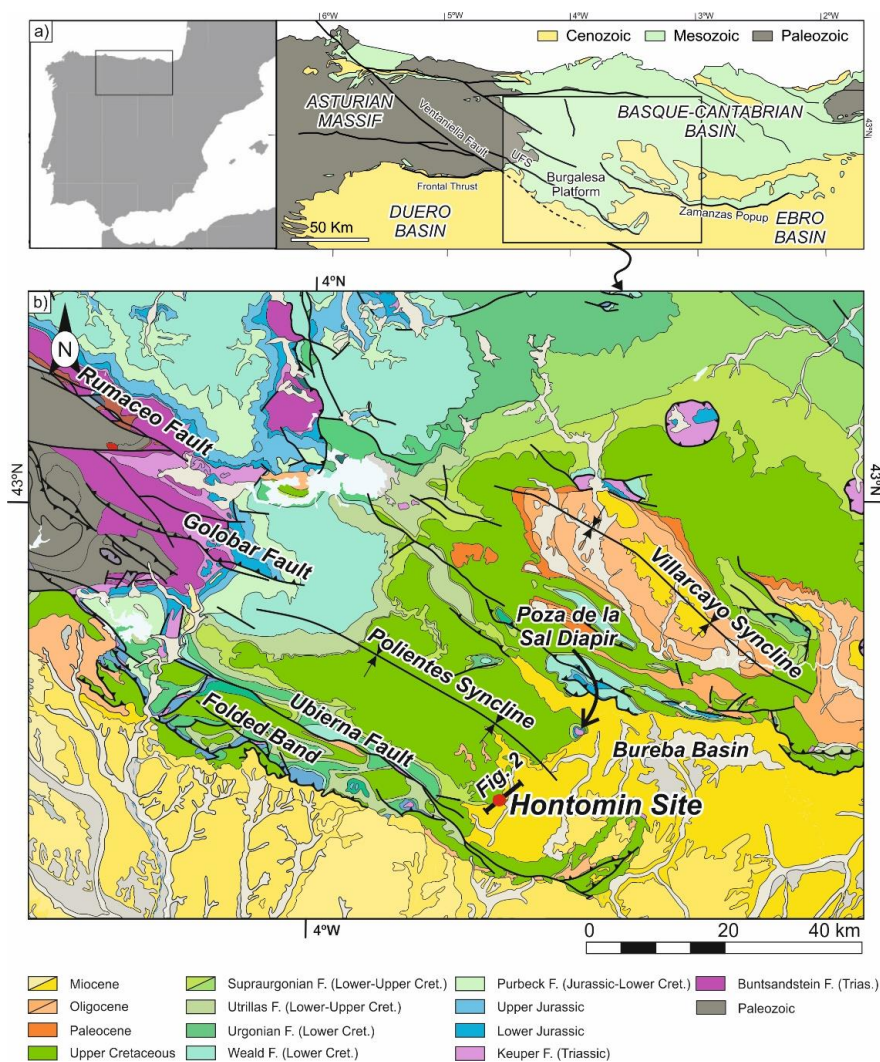
112

## 113 2. HONTOMÍN ONSHORE STUDY CASE

### 114 2.1 Geological description of the reservoir

115 The CO<sub>2</sub> storage site of Hontomín is enclosed in the southern section of the Mesozoic  
116 Basque–Cantabrian Basin, known as Burgalesa Platform (Serrano and Martínez del  
117 Olmo, 1990, Tavani, 2012), within the sedimentary Bureba Basin (**Fig. 1**). This  
118 geological domain is located in the northern junction of the Cenozoic Duero and Ebro  
119 basins, forming an ESE-dipping monocline bounded by the Cantabrian Mountains  
120 Thrust to the north, the Ubierna Fault System (UFS) to the south and the Asturian  
121 Massif to the west (**Fig. 1**).

122 The Meso-Cenozoic tectonic evolution of the Burgalesa Platform starts with a first rift  
123 period during Permian and Triassic times (Calvet et al., 2004; Dallmeyer and Martínez-  
124 García, 1990), followed by a relative tectonic quiescence during Early and Middle  
125 Jurassic times (e.g. Aurell et al., 2002). The main rifting phase took place during the  
126 Late Jurassic and Early Cretaceous times, due to the opening of the North Atlantic and  
127 the Bay of Biscay-Pyrenean rift system (García-Mondéjar et al., 1986; García-  
128 Mondéjar et al., 1996; Le Pichon and Sibuet, 1971; Lepvrier and Martínez-García,  
129 1990; Roca et al., 2011; Tugend et al., 2014). The convergence between Iberia and  
130 Eurasia from Late Cretaceous to Miocene times triggered the inversion of previous



131

132

133 *Figure 1. a) Location map of the study area in the Iberian Peninsula, along with the geological map of*

134 *the Asturian and Basque-Cantabrian areas, labelling major units and faults (modified after Quintà and*

135 *Tavani 2012); b) Geographical location of Hontomín pilot-plant (red dot) within the Basque-Cantabrian*

136 *Basin. This basin is tectonically controlled by the Ubierna Fault System (UFS; NW-SE oriented) and the*

137 *parallel Polientes syncline, the Duero and Ebro Tertiary basins and Poza de la Sal evaporitic diapir.*

138 *Cret: Cretaceous; F: Facies.*

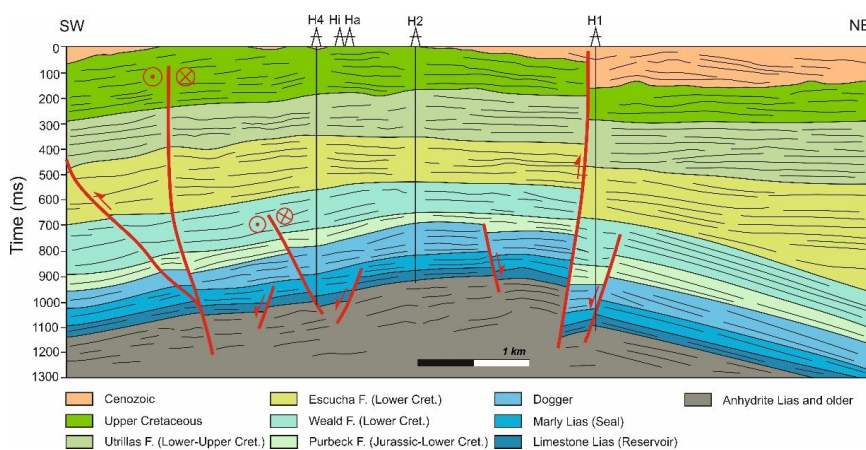
139



140

141 Mesozoic extensional faults and the development of a E-W orogenic belt (Cantabrian  
142 domain to the west and Pyrenean domain to the east) formed along the northern Iberian  
143 plate margin (Gómez et al., 2002; Muñoz, 1992; Vergés et al., 2002).

144 The facilities are located within the Basque-Cantabrian Basin (**Fig. 1b**). This reservoir  
145 is a deep saline aquifer developed in fractured Jurassic carbonates, with a low porous  
146 permeability matrix, located at almost 1,500 m depth (Alcalde et al., 2013). The  
147 Hontomín geological structure was described by Alcalde et al. (2013) and Le Gallo and  
148 de Dios (2018), and defined as a fold-related dome (Tavani et al., 2013). The reservoir  
149 structure is associated to the Cenozoic extensional tectonic stages, according to these  
150 authors. The present-day geological structure is related with the reactivation by a  
151 tectonic compressional phase during the Cenozoic Pyrenees compression (Alcalde et al.,  
152 2013).



153

154

155 *Figure 2: Interpretation of a 2D seismic reflection profile crossing the oil exploration wells (H1, H2 and*  
156 *H4), along with the monitoring well (Ha) and injection well (Hi) through Hontomin Pilot Plant (HPP).*  
157 *Modified from Alcalde et al. (2014). See Figure 1 for location, black line at the red circle.*

158



159 The Hontomín structure is bordered by the UFS to the south and west, by the Poza de la  
160 Sal diapir and the Zamanzas Popup structure (Carola, 2014) to the north and by the  
161 Ebro Basin to the east (**Fig. 1**). The structure has been classified as forced fold related  
162 dome structure (Tavani et al., 2013; **Fig. 2**), which was formed by an extensional fault  
163 system with migration of evaporites towards the hanging wall during the Mesozoic  
164 (Soto et al., 2011). During the tectonic compressional phase, associated with Cenozoic  
165 tectonics affecting the Pyrenees, the right-lateral transpressive inversion of the basement  
166 faults was activated, plus the reactivation of transverse extensional faults (**Fig. 2**; Tavani  
167 et al., 2013; Alcalde et al., 2014).

168

169 At the HPP, the target reservoir and seal formations consist of Lower Jurassic marine  
170 carbonates, arranged in an asymmetric dome-like structure (**Fig. 2**) with an overall  
171 extent of 15 km<sup>2</sup> and located at 1,485 m of depth (Alcalde et al., 2013, 2014; Ogaya et  
172 al., 2013). The target CO<sub>2</sub> injection point is a saline aquifer formed by a dolostone unit,  
173 known as “Carniolas”, and an oolitic limestone of the Sopeña Formation, both  
174 corresponding to Lias in time (Early Jurassic). The estimated porosity of the Carniolas  
175 reaches over 12% (Ogaya et al., 2013; Le Gallo and de Dios, 2018) and it is slightly  
176 lower at the Carbonate Lias level (8.5% in average). The reservoir levels contain saline  
177 water with more than 20 g/l of NaCl and very low oil content. The high porosity of the  
178 lower part of the reservoir (i.e., the Carniolas level) is the result of secondary  
179 dolomitization and different fracturing events (Alcalde et al., 2014). The minimum  
180 thickness of the reservoir units is 100 m. The potential upper seal unit comprises Lias  
181 marlstones and black shales from a hemipelagic ramp (**Fig. 2**); Pliensbachian and  
182 Toarcian) of the “Puerto del Pozazal” and Sopeña Formations.

183





184 *2.2 Regional tectonic field*

185 The tectonic context of HPP has been described from two different approaches: (1) the  
186 tectonic style of the fractures bordering the Hontomín reservoir (De Vicente et al., 2011;  
187 Tavani et al., 2011) and (2) the tectonic regional field described from earthquakes with  
188 mechanism solutions and GPS data (Herraiz et al., 2000; Stich et al., 2006; De Vicente  
189 et al., 2008).

190 (1) The tectonic style of the Bureba Basin was described by De Vicente et al. (2011),  
191 which classified the Basque-Cantabrian Cenozoic Basin (**Fig. 1a**) as transpressional  
192 with contractional horsetail splay basin. The NW-SE oriented Ventaniella fault (**Fig.**  
193 **1a**), includes the UFS in the southeastward area, being active between the Permian and  
194 Triassic period, and strike-slip during the Cenozoic contraction. In this tectonic  
195 configuration, the Ubierna Fault is a right-lateral strike-slip fault. These authors pointed  
196 out the sharp contacts between the thrusts and the strike-slip faults in this basin.  
197 Furthermore, Tavani et al. (2011) also described complex Cenozoic tectonic context  
198 where right-lateral tectonic style reactivated WNW-ESE trending faults. Both the  
199 Ventaniella and the Ubierna faults acted as transpressive structures forming 120 km  
200 long and 15 km wide of the UFS, and featured by 0.44 mm/yr of averaged tectonic  
201 strike-slip deformation between the Oligocene and the present day. The aforementioned  
202 authors described different surface segments of the UFS of right-lateral strike-slip  
203 ranging between 12 and 14 km length. The structural data collected by Tavani et al.  
204 (2011) pointed out the 60% of data correspond to right lateral strike-slip with WNW-  
205 ESE trend, together with conjugate reverse faulting with NE-SW, NW-SE and E-W  
206 trend, and left-lateral strike-slip faults N-S oriented. They concluded that this scheme  
207 could be related to a transpressional right-lateral tectonic system with a maximum  
208 horizontal compression,  $S_{Hmax}$ , striking N120°E. Concerning the geological evidence of



209 recent sediments affected by tectonic movements of the UFS, Tavani et al. (2011)  
210 suggest Middle Miocene in time for this tectonic activity. However, geomorphic  
211 markets (river and valley geomorphology) could indicate activity at present-times. All  
212 of these data correspond to regional or small-scale data collected to explain the Basque-  
213 Cantabrian Cenozoic transpressive basin. The advantage of the methodology proposed  
214 here to establish the tectonic local regime affecting the reservoir, is the searching for  
215 local-scale tectonics (20 km sized), and the estimation of the depth for the non-  
216 deformation surface for strata folding in transpressional tectonics (Lisle et al., 2009).

217 (2) Regarding the stress field from earthquake focal mechanism solutions, Herraiz et al.  
218 (2000) pointed out the regional trajectories of  $S_{Hmax}$  with NNE-SSW trend, and with a  
219 NE-SW  $S_{Hmax}$  trend from slip-fault inversion data. Stich et al. (2006) obtained the stress  
220 field from seismic moment tensor inversion and GPS data. These authors pointed out a  
221 NW-SE Africa-Eurasia tectonic convergence at tectonic rate of 5 mm/yr approximately.  
222 However, no focal mechanism solutions are found within the Hontomín area (20 km)  
223 and only long-range spatial correlation could be made with high uncertainty (in time,  
224 space and magnitude). The same lack of information appears in the work of De Vicente  
225 et al. (2008), with no focal mechanism solutions in the 50 km surrounding the HPP. In  
226 this work, these authors classified the study area as uniaxial extension to strike-slip with  
227 NW-SE  $S_{Hmax}$  trend.

228 Regional data about the tectonic field within the HPP (Bureba basin), inferred from  
229 different works (Herraiz et al., 2000; Stich et al., 2006; De Vicente et al., 2008, 2011;  
230 Tavani et al., 2011; Tavani, 2012), show differences for the  $S_{Hmax}$  trend. These works  
231 explain the tectonic framework for regional scale, nevertheless local tectonics could  
232 determine the low permeability and the potential Induced Seismicity within the  
233 Hontomín reservoir. In the next section, we have applied the methodology described at



234 the section 3 of this manuscript, in order to compare the regional results from these  
235 works and to establish the tectonic evolution of the Burgalesa Platform.

236

### 237 *2.3 Strategy of the ENOS European Project*

238 Hontomín pilot-plant (HPP) for CO<sub>2</sub> onshore storage is the only one in Europe  
239 recognized as a key-test-facility, and it is managed and conducted by CIUDEN  
240 (*Fundación Ciudad de la Energía*). This HPP is located within the province of Burgos  
241 (**Fig. 1b**), in the northern central part of Spain.

242 The methodology proposed in this work and its application for long-term onshore CCS  
243 managing in the frame of geological risk, is based on the strain tensor calculation, as  
244 part of the objectives proposed in the European project ENOS. The ENOS project is an  
245 initiative of CO<sub>2</sub>GeoNet, the European Network of Excellence on the geological storage  
246 of CO<sub>2</sub> for supporting onshore storage and fronting the associated troubles as CCS  
247 perception, the safe storage operation, potential leaking management and health, and  
248 environmental safety (Gastine et al., 2017). ENOS combines a multidisciplinary  
249 European project, which focuses in onshore storage, with the demonstration of best  
250 practices through pilot-scale projects in the case of Hontomín facilities. Moreover, this  
251 project claims for creating a favorable environment for CCS onshore through public  
252 engagement, knowledge sharing, and training (Gastine et al., 2017). In this context, the  
253 work-package WP1 is devoted to “ensuring safe storage operations”. The IGME team is  
254 committed to develop and to carry out a technology to determine the active strain-field  
255 affecting the sub-surface reservoir and fault patterns and to assign the fault type for the  
256 estimation of potential fault-patterns as low-permeability paths as well.

257

258



259 3. METHODS AND RATIONALE

260 The lithosphere remains in a permanent state of deformation, related to plate tectonics  
261 motion. Strain and stress fields are the consequence of this deformation on the upper  
262 lithosphere, arranging different fault patterns that determine sedimentary basins and  
263 geological formations. Kinematics of these faults describes the stress/strain fields, for  
264 example measuring grooves and slickensides on fault planes (see Angelier, 1979,  
265 Reches, 1983 among others). The relevance of the tectonic field is that stress and strain  
266 determine the earthquake occurrence by the fault activity. In this work, we have  
267 performed a brittle analysis of the fault kinematics, by measuring slickenfiber on fault  
268 planes in several outcrops in the surroundings of the onshore reservoir. These faults  
269 were active during the Mesozoic, and from Late Miocene to Quaternary. To carry out  
270 the methodology proposed in this work, the study area was divided in a circle with four  
271 equal areas, and we searched outcrops of fresh rock to perform the fault kinematic  
272 analysis. This allows establishing a realistic tectonic very-near field to be considered  
273 during the storage seismic monitoring and long-term management.

274

275 2.1 *Paleostrain Analysis*

276 We have applied the strain inversion technique to reconstruct the tectonic field  
277 (paleostrain evolution), affecting the Hontomín site between the Triassic, Jurassic,  
278 Cretaceous and Neogene ages (late Miocene to present times). For a further  
279 methodology explanation see Etchecopar et al. (1981), Reches (1983) and Angelier  
280 (1990). The main assumption for the inversion technique of fault population is the self-  
281 similarity to the scale invariance for the stress/strain tensors. This means that we can  
282 calculate the whole stress/strain fields by using the slip data on fault planes and for  
283 homogeneous tectonic frameworks. The strain tensor is an ellipsoid defined by the



284 orientation of the three principal axes and the shape of the ellipsoid ( $k$ ). This method  
285 assumes that the slip-vectors, obtained from the pitch of the striation on different fault  
286 planes, define a common strain tensor or a set in a homogeneous tectonic arrangement.  
287 We assume that the strain field is homogeneous in space and time, the number of faults  
288 activated is greater than five and the slip vector is parallel to the maximum shear stress  
289 ( $\tau$ ).

290 The inversion technique is based on the Bott equations (Bott, 1959). These equations  
291 show the relationship between the orientation and the shape of the stress ellipsoid:

292

$$293 \quad \tan(\theta) = [n / (l * m)] * [m^2 - (1 - n^2) * R'] \quad [\text{eq.1}]$$

$$294 \quad R' = (\sigma_z - \sigma_x) / (\sigma_y - \sigma_x) \quad [\text{eq.2}]$$

295

296 Where  $l$ ,  $m$  and  $n$  are the direction cosines of the normal to the fault plane,  $\theta$  is the pitch  
297 of the striation and  $R'$  is the shape of the stress ellipsoid obtained in an orthonormal  
298 coordinate system,  $x$ ,  $y$ ,  $z$ . In this system,  $\sigma_y$  is the maximum horizontal stress,  $\sigma_x$  is the  
299 minimum horizontal stress axis and  $\sigma_z$  is the vertical stress axis.

300

### 301 *3.2 The Right-Dihedral Model for Paleostrain Analysis*

302 The Right-Dihedral (RD) is a semi-quantitative method based on the overlapping of  
303 compressional and extensional zones by using a stereographic plot. The final plot is an  
304 interferogram figure which usually defined the strain-regime. This method is strongly  
305 robust for conjugate fault sets and with different dip values for a same tensor. The RD  
306 was originally defined by Pegoraro (1972) and Angelier and Mechler (1977), as a  
307 geometric method, adjusting the measured fault-slip data (slickensides) in agreement  
308 with theoretical models for extension and compressive fault-slip. Therefore, we can



309 constraint the regions of maximum compression and extension related to the strain  
310 regime.

311

### 312 *3.3 The Slip Model for the Paleostrain Analysis*

313 The Slip Model (SM) is based on the Navier-Coulomb fracturing criteria (Reches,  
314 1983), taking the Anderson model solution for this study (Anderson, 1951; Simpson,  
315 1997). The Anderson model represents the geometry of the fault plane as monoclinic,  
316 relating the quantitative parameters of the shape parameter ( $K'$ ) with the internal  
317 frictional angle for rock mechanics ( $\phi$ ) (De Vicente 1988, Capote et al., 1991).  
318 Moreover, this model is valid for neoformed faults, and some considerations have to be  
319 accounted for previous faults and weakness planes present in the rock. These  
320 considerations are related to the dip of normal and compressional faults, such as for  
321 compressional faulting values lower than  $b < 45^\circ$ , reactivated as extensional faults. This  
322 model shows the relationships between the  $K'$ ,  $\phi$  and the direction cosines for the  
323 striation on the fault plane (De Vicente, 1988; Capote et al., 1991):

324

$$325 \quad K' = e_y / e_z \quad [eq.3]$$

326

327 Where  $e_z$  is the vertical strain axis,  $e_y$  is the maximum horizontal shortening and  $e_x$  is  
328 the minimum horizontal shortening. This model assumes that there is no change of  
329 volume during the deformation and  $e_y = e_x + e_z$ .

330 For isotropic solids, principal strain axes coincide with the principal stress axes. This  
331 means that in this work, the orientation of the principal stress axis,  $S_{Hmax}$  is parallel to  
332 the orientation of the principal strain axes,  $e_y$ , and hence, the minimum stress axis,  $S_{hmin}$ ,



333 is parallel to the minimum strain axis,  $e_x$ . This assumption allows us to estimate the  
334 stress trajectories ( $S_{Hmax}$  and  $S_{hmin}$ ) from the  $De_y$  SM results.

335 Resolving the equations of Anderson (Anderson, 1951) for different values, we can  
336 classify the tectonic regime that activates one fault from the measurement of the fault  
337 dip, sense of dip and pitch of the slickenside, assuming that one of the principal axes  
338 ( $e_x$ ,  $e_y$  or  $e_z$ ) are vertical (Angelier, 1984). We can classify of the tectonic regime and  
339 represent the strain tensor by using the  $e_y$  and  $e_x$  orientation.

340

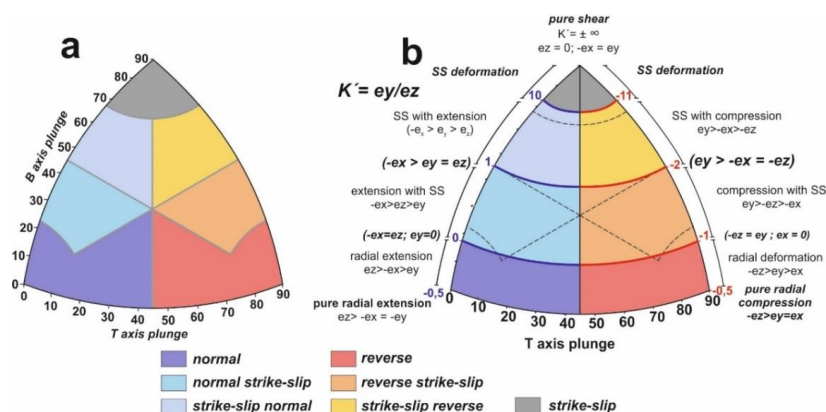
#### 341 *3.4 The $K'$ strain diagram*

342 Another analysis can be achieved by using the  $K'$ -strain diagram developed by Kaverina  
343 et al. (1996) and codified in python-code by Álvarez-Gómez (2014). These authors have  
344 developed a triangular representation based on the fault-slip, where tectonic patterns can  
345 be discriminated between strike-slip and dip-slip types. This diagram is divided in 7  
346 different zones according to the type of fault: (1) pure normal, (2) pure reverse and (3)  
347 pure strike-slip, combined with the possibility of oblique faults: (4) reverse strike-slip  
348 and (5) strike-slip with reverse component, and lateral faults: (6) normal strike-slip and  
349 (7) strike-slip faults with normal component (**Fig. 3**). Strike-slip faults are defined by  
350 small values for pitch ( $p < 25^\circ$ ) and dips close to vertical planes ( $\beta > 75^\circ$ ). High pitch  
351 values ( $p > 60^\circ$ ) are related to normal or/reverse fault-slip vectors. Extensional faults  
352 show  $e_y$  in vertical whereas compressional faults show  $e_y$  in horizontal plane.

353 This method was originally performed for earthquake focal mechanism solutions by  
354 using the focal parameters, the nodal planes (dip and strike) and rake. The triangular  
355 graph is based on the equal-areal representation of the T, N or B and P axes in spherical  
356 coordinates (T tensile, N or B neutral and P pressure axes), and the orthogonal  
357 regression between  $M_s$  and  $m_b$  for the Harvard earthquake CMT global catalogue in



1996. Álvarez-Gómez (2014) presented a code python-based for computing the  
 Kaverina diagrams, and we have modified the input parameters by including the  $K'$   
 intervals for the strain field from the SM. The relationship between the original diagram  
 of Kaverina (Fig. 3a) and the  $K'$ -dip diagram (Fig. 3b) that we have used in this work is  
 shown in the figure 3. The advantage of this diagram is the fast assignation of the type  
 of fault and the tectonic regime that determine this fault pattern, and the strain axes  
 relationship.



365  
 366 Figure 3. a) Kaverina original diagram to represent the tectonic regime from an earthquake focal  
 367 mechanism population (see Kaverina et al., 1996 and Álvarez-Gómez, 2014). b)  $K'$ -strain diagram used  
 368 in this work. Dotted lines represent the original Kaverina limits. Colored zones represent the type of  
 369 fault. The tectonic regime is also indicated by the relationship between the strain axes and the colored  
 370 legend. SS Strike slip. The B axis is the orthogonal to the P and T axes.

371  
 372 Table 1 summarizes the different tectonic regimes of the figure 3b showing the  
 373 relationship with the strain main axes  $e_y$ ,  $e_x$  and  $e_z$ . This diagram exhibits a great  
 374 advantage to classify the type of fault according to the strain tensor. Therefore, we can  
 375 assume the type of fault from the fault orientation affecting geological deposits for each  
 376 strain tensor obtained.

377





$K'$	$T$ -axis	strain axis rel.	fault type	tectonic field
$< -0.5$	$0^\circ$	$e_z > e_x = -e_y$	normal	pure radial extension
$-0.5 < K' < 0$	$0^\circ-45^\circ$	$e_z > e_x > e_y$	normal	radial extension
$K' = 0$	$0^\circ-45^\circ$	$e_z = -e_x, e_y = 0$	normal	plain strain
$0 < K' < 1$	$0^\circ-45^\circ$	$-e_x > e_z > e_y$	normal with SS	extension with shear
$k=1$	$0^\circ-45^\circ$	$-e_x > e_y = e_z$	normal with SS	extension with shear
$1 < K' < 10$	$0^\circ-45^\circ$	$-e_x > e_y > e_z$	strike-slip with N	shear with extensional
$10 < K' < \infty$	$0^\circ-45^\circ$	-----	strike-slip	shear deformation
$K' = \infty$	$45^\circ$	$e_z = 0; -e_x = e_y$	strike-slip	pure shear deformation
$\infty < K' < -11$	$45^\circ-90^\circ$	-----	strike-slip	shear deformation
$-11 < K' < -2$	$45^\circ-90^\circ$	$e_y > -e_x > -e_z$	strike-slip with R	shear with compression
$K' = -2$	$45^\circ-90^\circ$	$e_y > -e_x = -e_z$	reverse with SS	compression with shear
$-2 < K' < -1$	$45^\circ-90^\circ$	$e_y > -e_z > -e_x$	reverse with SS	compression with shear
$K' = -1$	$45^\circ-90^\circ$	$-e_z = e_y, e_x = 0$	reverse	plain strain
$-1 < K' < -0.5$	$45^\circ-90^\circ$	$-e_z > e_y > e_x$	reverse	radial compression
$K' = -0.5$	$45^\circ-90^\circ$	$-e_z > e_y = e_x$	reverse	pure radial compression

SS = strike-slip  
 N = normal  
 R = reverse

$e_x$  = value of the minimum horizontal shortening  
 $e_y$  = value of the maximum horizontal shortening  
 $e_z$  = value of the vertical axis

378

379 *Table 1. Different tectonic regimes,  $K'$  values, dip values and fault type for the Kaverina modified*  
 380 *diagram used in this work. According to the strain axes relationship, faults can be classified and the*  
 381 *tectonic regime can be established.*

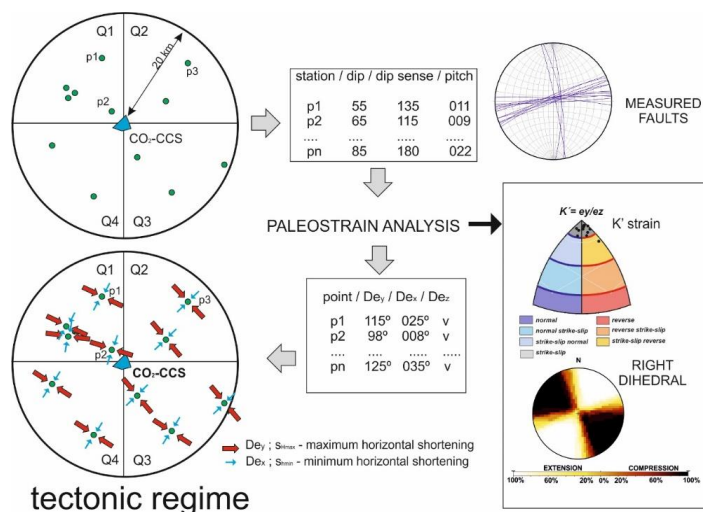
382

### 383 3.5 The Circular-Quadrant-Search (CQS) strategy for the paleostrain analysis

384 In this work, we propose a low-cost strategy based on a well-known methodology for  
 385 determining the stress/strain tensor affecting a CCS reservoir, which will allow for  
 386 monitoring long-term geological and seismic behavior. The objective is to obtain  
 387 enough structural data and spatially homogeneous of faults (**Figs. 4, 5**), for  
 388 reconstructing the stress/strain tensor by using the methodologies described above. The  
 389 key-point is the determination of the orientation of the  $e_y$ ,  $e_x$  and  $K'$  to plot in a map and  
 390 therefore, to establish the tectonic regime. We have chosen quadrants of the circles with  
 391 the aim to obtain a high-quality spatial distribution of point for the interpretation of the



392 local and very near strain field. Hence, data are homogeneously distributed, instead of  
 393 being only concentrated in one quadrant of the circle.



394 tectonic regime

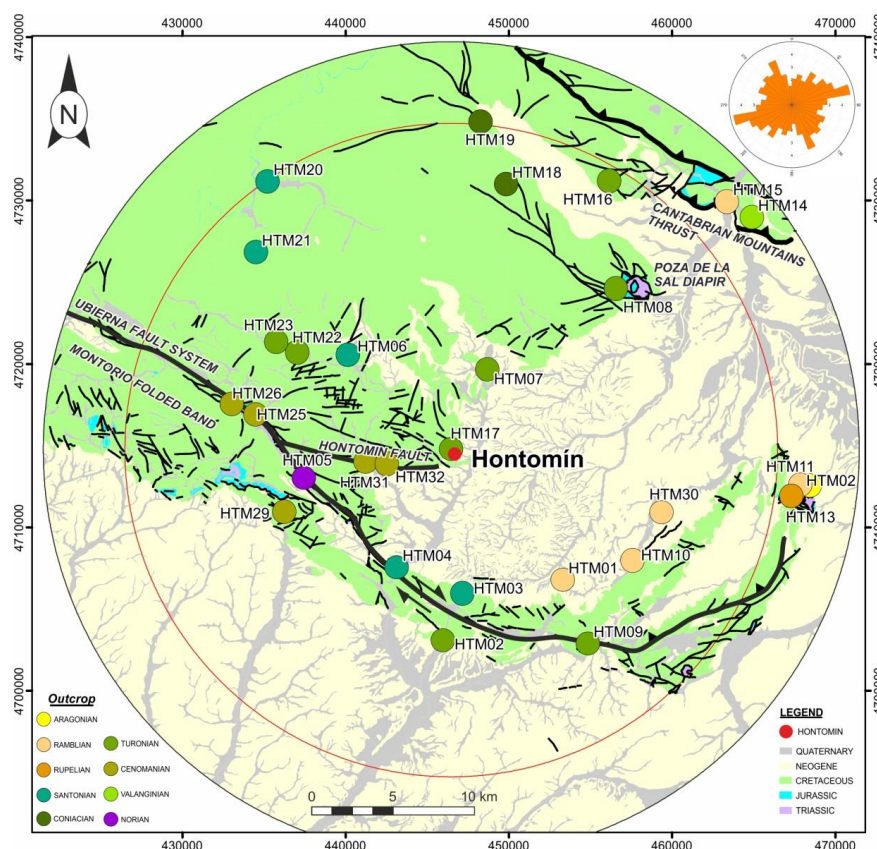
395 Figure 4. Methodology proposed to obtain the strain field affecting the CCS reservoir. The distances for  
 396 outcrops and quadrants proposed is 20 km. The technique of Right Dihedral and the  $K'$  strain diagram is  
 397 described in the main text. The  $e_y$  and  $e_x$  represented are a model for explaining the methodology.  $De_y$   
 398 and  $De_x$  are the direction of the maximum and minimum strain, respectively. Blue box at the center is the  
 399  $CO_2$  storage geological underground formation.

400

401 Pérez-López et al. (2018) carried out a first approach to the application of this  
 402 methodology at Hontomín, under the objective of the ENOS project (see next section  
 403 for further details). We propose a circular searching of structural field stations (Figs. 4,  
 404 5), located within a 20 km radius. This circle was taken given that active faults with the  
 405 capacity of triggering earthquakes of magnitudes close to M 6, exhibits a surface rupture  
 406 of tens of kilometers, according to the empirical models (Wells and Coppersmith,  
 407 1994). Moreover, Verdon et al. (2015) pointed out that the maximum distance of  
 408 induced earthquakes for fluid injection is 20 km. Larger distances could not be related  
 409 to the stress/strain regime within the reservoir, except for the case of large geological



410 structures (folds, master faults, etc.). Microseismicity in CCS reservoir is mainly related  
411 to the operations during the injection/depletion stages and long-term storage (Verdon  
412 2014, Verdon et al., 2015, McNamara, 2016).



413  
414 *Figure 5. Geographical location of field outcrops in the eastern part of the Burgalesa Platform domain.*  
415 *Black lines: observed faults; red circle: 20km radius study zone. A total of 447 fault data were collected*  
416 *in 32 outcrops. Data were measured by a tectonic compass on fault planes at outcrops. The spatial*  
417 *distribution of the field stations is constrained by the lithology. Coordinates are in meters, UTM H30.*

418  
419 The presence of master faults (capable to trigger earthquakes of magnitude = or > than 6  
420 and 5 km long segment) inside the 20 km radius circle, implicates that the regional  
421 tectonic field is relevant for the reservoir geodynamics, being responsible for the strain  
422 accumulation in kilometric fault-sized. Furthermore, the presence of master faults could



423 increase the occurrence of micro-earthquakes, due to the presence of secondary faults  
424 prone to trigger earthquakes by their normal seismic cycle. Bearing in mind that CCS  
425 onshore reservoirs use to be deep saline aquifers (e.g. Bentham and Kirby, 2005), as  
426 Hontomín is (Gastine et al., 2017, Le Gallo and de Dios, 2018), and be related to  
427 folding and fractured deep geological structures, local tectonics plays a key role in  
428 micro-seismicity and the possibility of CO<sub>2</sub> leakage.

429 The constraints of this strategy are related to the absence of kinematics indicators on  
430 fault planes, due to the geomechanical property of the lithology involved or the erase by  
431 later geological processes as neoformed mineralization, etc. A poor spatial distribution  
432 of the outcrops was also taken into account for constraining the strategy. The age of  
433 sediments does not represent the age of the active deformations and hence, the active  
434 deformation has to be analyzed by performing alternative methods (i.e.  
435 paleoseismology, archaeoseismology).

436

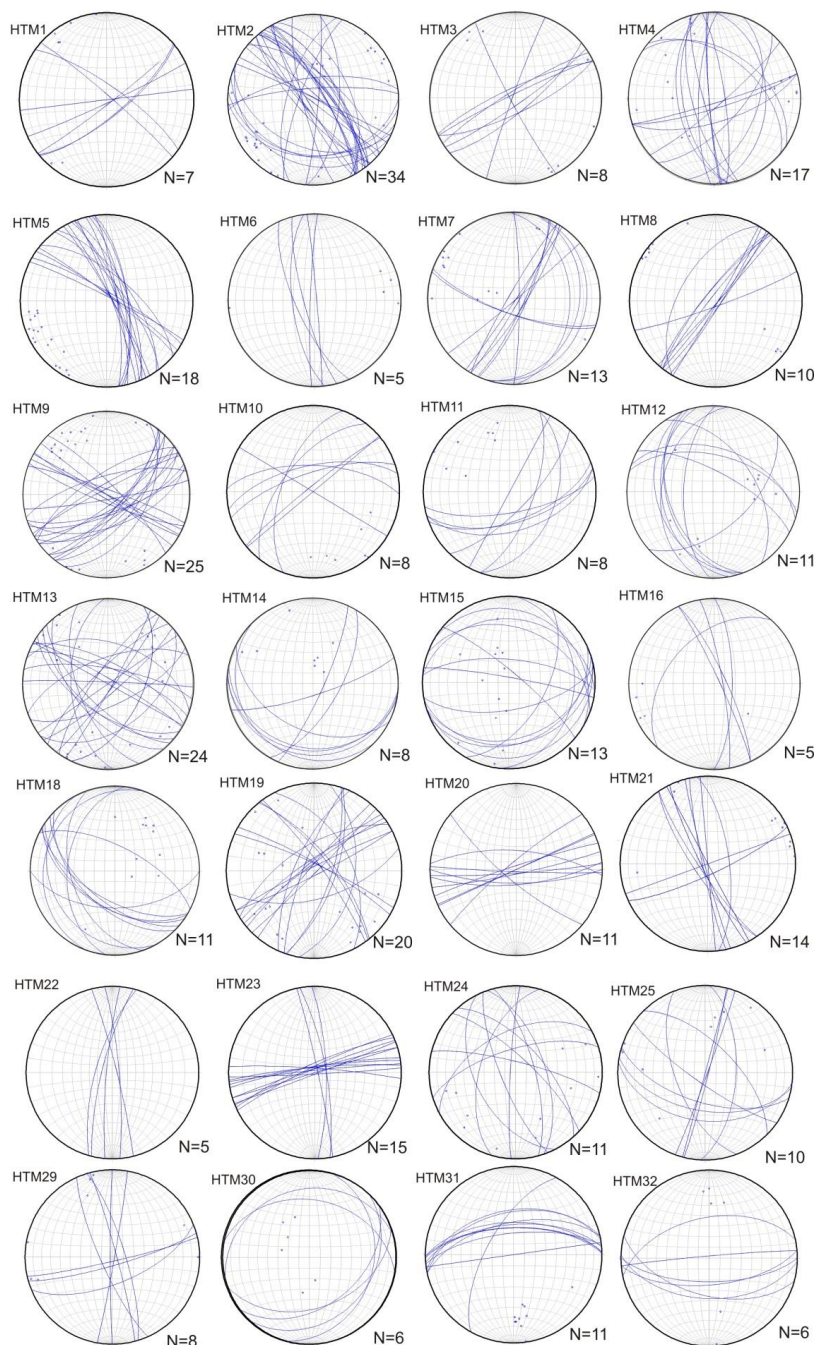
## 437 4. RESULTS

### 438 4.1 Strain Field Analysis

439 We have collected 447 fault-slip data on fault planes in 32 outcrops, located within a 20  
440 km radius circle centered at the HPP (**Fig. 5**). The age of the structural field stations  
441 ranges between Early Triassic to present-day and are mainly located in Cretaceous  
442 limestones and dolostones (**Fig. 5, Table 2**). No Jurassic outcrops were located, and  
443 seven stations are located on Neogene sediments, ranging between Early Oligocene to  
444 Middle-Late Miocene. The short number of Neogene stations is due to the mechanical  
445 properties of the affected sediments, mainly poor-lithified marls and soft-detrital fluvial  
446 deposits. Despite that, all the Neogene stations exhibit high-quality data with a number  
447 of fault-slip data ranging between 7 and 8, enough for a minimum quality analysis.



448 We have labeled the outcrops with the acronym HTM followed by a number (see **figure**  
449 **5** for the geographical location and **Table 2** and **figure 6** for the fault data). The station  
450 with the highest number of faults measured is HTM17 with 107 faults on Cretaceous  
451 limestone. Nevertheless, we have removed the HTM17 to the analysis due to the high  
452 number of measurements, including lot of noise that could disturb the whole analysis.  
453 Conjugate fault systems can be recognized in most of the stations (HTM1, 3, 5, 7, 10,  
454 14, 16, 21, 23, 25, 26, 29, 30 and 32, **Fig. 6**), although there are a few stations with only  
455 one well defined fault set (6, 22, 32). We have to bear in mind that recording of  
456 conjugate fault systems are more robust for the brittle analysis than recording isolated  
457 fault sets, better constraining the solution (Žaholar and Vrabec, 2008). In total, 29 of 32  
458 stations were used (HTM24, 27, 28 with no quality data), and from these 29 stations, 24  
459 were analyzed with the paleostrain technique. Solutions obtained here are robust to  
460 establish the strain field as the orientation of the  $e_y$ ,  $S_{Hmax}$  (**Figs. 7 and 8**).



461

462 *Figure 6. Stereographic representation (cyclographic plot in Schmidt net, lower hemisphere) of the fault*

463 *planes measured in the field stations. “n” is the number of available data for each geostructural station.*

464 *HTM24, 27, 28 are not included due to lack of data, and HTM17 due to the high number of faults.*

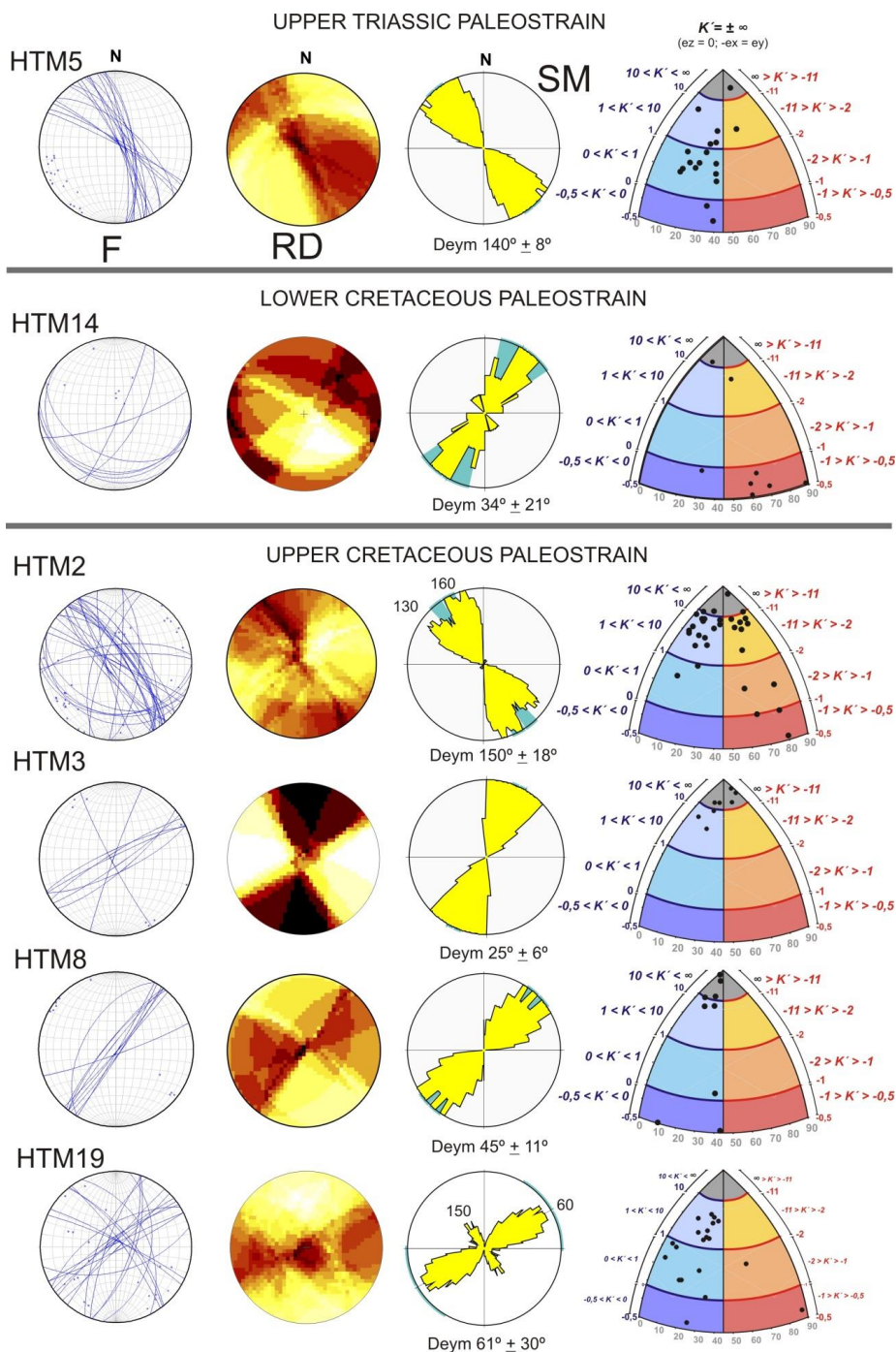


465

466 The results obtained from the application of the paleostrain method have been expressed  
467 in stereogram, right dihedral (RD), slip method (SM) and  $K'$ - diagram (**Fig. 7**). The  $K'$ -  
468 diagram shows the fault classification as normal faults, normal with strike-slip  
469 component, pure strike-slip, strike-slip with reverse component and reverse faults (see  
470 **Fig. 3**). Main faults are lateral strike-slips and normal faults, followed by reverse faults,  
471 strike-slips and oblique strike-slips faults. The results of the strain regime are as  
472 follows: 1) 43% of extensional with shear component; 2) 22% of shear; 3) 13% of  
473 compressive strain (lower Cretaceous and early-middle Miocene, **Table 2**); 4)13% of  
474 pure shear and 5) 9% of shear with compression strain field, although with the presence  
475 of five reverse faults.

476 On the other hand, we can observe that there are solutions with a double value for the  
477  $e_y$ ,  $S_{Hmax}$  orientation: HTM1, 2, 10, 11, 13, 15, 19, 26, and 30. The stations HTM3 and  
478 23 (upper Cretaceous), show the best solution for strike-slip strain field as a pure strike-  
479 slip regime and  $e_y$  with N25°E and N99°E trend, respectively (**Fig. 7**).

480 It is easy to observe the agreement between the  $e_y$  results from the SM and the  $K'$ - strain  
481 diagram, for instance, in the HTM 2 the  $K'$ -diagram indicates strike-slip faults with  
482 reverse component for low dips ( $0^\circ < \beta < 40^\circ$ ) but also indicates strike-slip faults with  
483 normal component for larger dips ( $40^\circ < \beta < 90^\circ$ ). However, both results are in  
484 agreement with a strain field defined by the orientation for  $e_y$ ,  $S_{Hmax}$  with  $N150^\circ \pm 18^\circ$   
485 trend. This tectonic field affects Cretaceous carbonates and coincides with the regional  
486 tectonic field proposed by Herraiz et al. (2000), Stich et al. (2006),Tavani et al. (2011)  
487 and Alcalde et al. (2014).





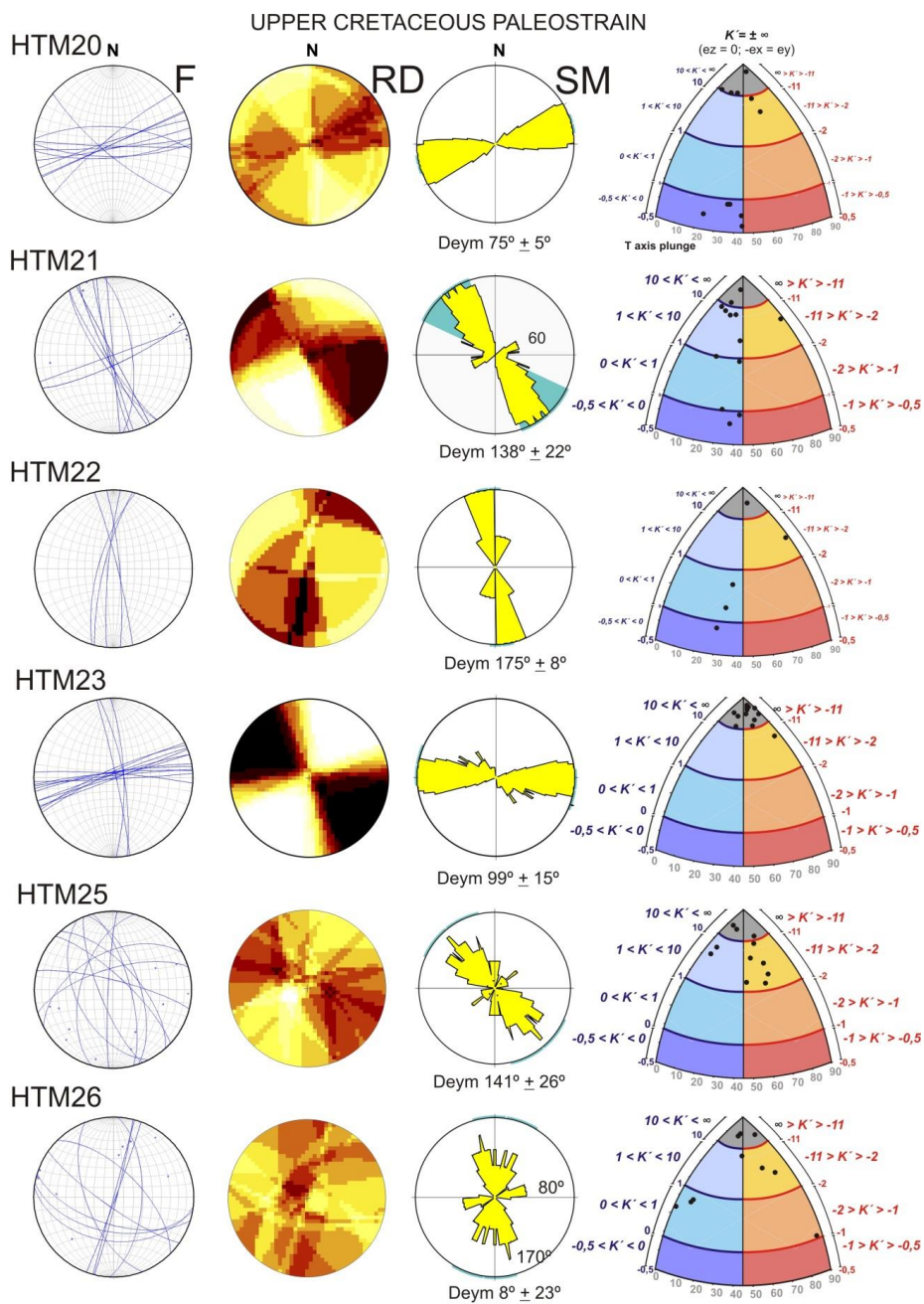


**FIGURE 7b**

489

490

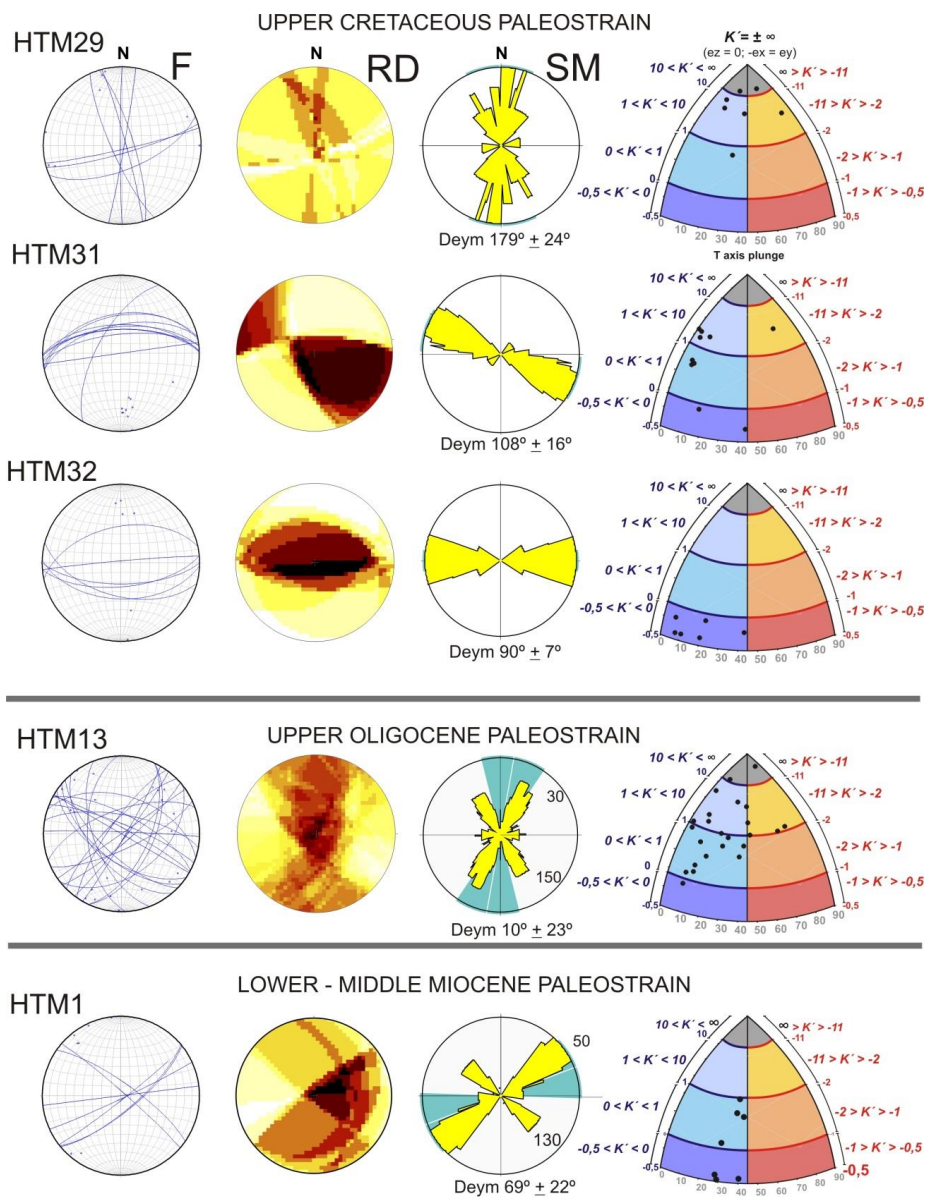
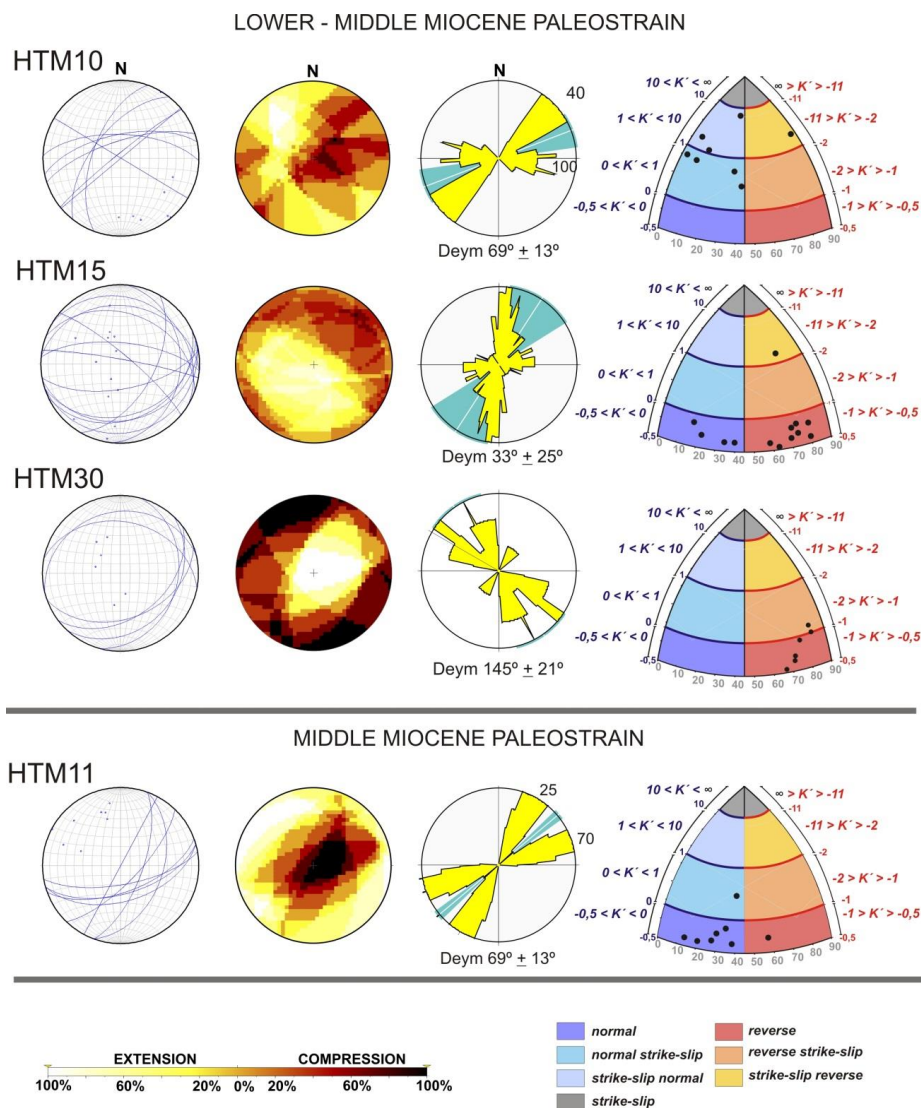


**FIGURE 7c**



492

493

494 *Figure 7. Results of the paleostrain analysis obtained and classified by age. Deym: striking of the*  
 495 *averaged of the  $D_e$  value; F: fault stereographic representation;  $K'$ : diagram with dots for each fault*  
 496 *slip solution; RD: Right Dihedral method; SM: Slip Method,  $K'$ . See Methods for further explanation.*

497

**FIGURE 7d**



STATION	n° faults	series/epoch	Dey main direction	dispersion	strain tensor
HTM05	18	UPPER TRIASSIC	140	8	NORMAL STRIKE-SLIP
HTM14	8	LOWER CRETACEOUS	34	21	COMPRESSION
HTM02	34	UPPER CRETACEOUS	150	18	STRIKE-SLIP (N-C)
HTM03	8	UPPER CRETACEOUS	25	6	STRIKE-SLIP (N-C)
HTM08	10	UPPER CRETACEOUS	45	11	STRIKE-SLIP
HTM17	105	UPPER CRETACEOUS	107	24	NORMAL
HTM19	20	UPPER CRETACEOUS	61	30	NORMAL STRIKE-SLIP
HTM20	11	UPPER CRETACEOUS	75	5	STRIKE-SLIP
HTM21	14	UPPER CRETACEOUS	138	22	STRIKE-SLIP NORMAL
HTM22	5	UPPER CRETACEOUS	175	8	NORMAL STRIKE-SLIP
HTM23	14	UPPER CRETACEOUS	99	15	STRIKE-SLIP
HTM25	11	UPPER CRETACEOUS	141	26	STRIKE-SLIP COMPRESSION
HTM26	10	UPPER CRETACEOUS	0	23	STRIKE-SLIP
HTM29	8	UPPER CRETACEOUS	179	24	STRIKE-SLIP NORMAL
HTM31	11	UPPER CRETACEOUS	108	16	STRIKE-SLIP NORMAL
HTM32	6	UPPER CRETACEOUS	90	7	NORMAL
HTM13	24	EARLY OLIGOCENE	25-160	23	NORMAL STRIKE-SLIP
HTM01	7	EARLY-MIDDLE MIOCENE	70	22	NORMAL STRIKE-SLIP
HTM10	8	EARLY-MIDDLE MIOCENE	69	13	NORMAL STRIKE-SLIP
HTM15	13	EARLY-MIDDLE MIOCENE	33	25	COMPRESSION
HTM30	6	EARLY-MIDDLE MIOCENE	145	21	COMPRESSION
HTM11	8	MIDDLE MIOCENE	50	4	NORMAL STRIKE-SLIP

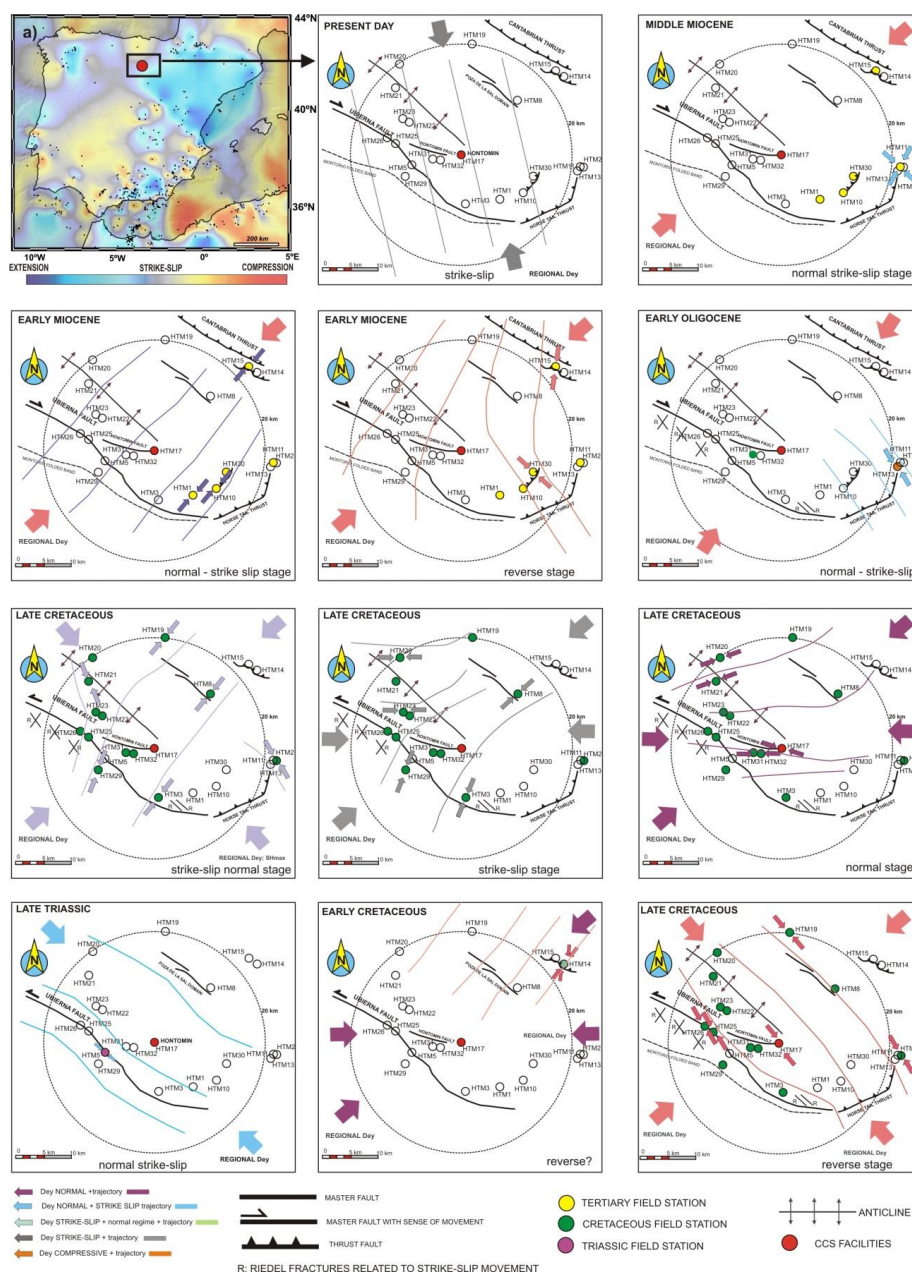
498

499 *Table 2. Summary of the outcrops showing the number of faults, the type of the strain tensor obtained, the*  
 500 *De<sub>y</sub>, S<sub>Hmax</sub> striking and the age of the affected geological materials. Asterisk indicates those field stations*  
 501 *detailed in the figure 7. N-C is normal component for strike-slip movement.*

502

503 Two e<sub>y</sub>, S<sub>Hmax</sub> directions can be considered, N150°E and N50°E. We obtained an  
 504 averaged value of N105°E by mixing both values of trend. However, a large number of  
 505 measured faults and their uncertainties slightly disturb the results (**Table 2**).

506



507

508 *Figure 8) Upper left frame: Synthesis of the  $K'$ -map obtained from Giner-Robles et al. (2018) for the*  
 509 *whole Iberian Peninsula from focal mechanism solutions. HPP is located between a triple junction of  $K'$*   
 510 *defined by compression towards the north, extension to the southeast and strike-slip to the west. Black*  
 511 *dots are the earthquakes with focal mechanism solutions used. Sketches represent the  $e_y$ ,  $S_{Hmax}$*   
 512 *trajectories obtained from the outcrops for early Triassic, Early Cretaceous, Late Cretaceous, Early*



513 *Oligocene, Early – Middle Miocene and Present-day strain field from Herraiz et al. (2000). Main*  
514 *structures activated under the strain field defined are also included.*

515

#### 516 *4.2 Late Triassic Paleostrain*

517 Strain analysis from HTM5 fault set shows  $e_y$  with NW-SE trending and shear regime  
518 with extension defined by strike-slip faults (**Figs. 7a and 8**). This is in agreement with  
519 the uniaxial extension described in Tavani (2012), author that constrain this regime with  
520  $S_{\text{hmin}}$  with NE-SW trending.

521

#### 522 *4.3 Cretaceous Paleostrain*

523 HTM 14 is the only outcrop from early Cretaceous age, showing a compressive tectonic  
524 stage with reverse fault solutions, defined by  $e_y$  with NE-SW trending (**Fig. 8**). Taking  
525 into account the extensional stage related to the Main Rifting Stage (i.e. Carola, 2004;  
526 Tavani, 2012; Tugend et al., 2014) during this age, we interpreted these results as a  
527 modern strain field, probably related to the Cenozoic Inversion stage. A local  
528 compressive stage was discarded due to the absence of compressive structures related to  
529 this age in the area and surroundings.

530 Outcrops HTM 2, 17, 19, 20, 21, 23, 25, 26, 29, 31 and 32 are from the upper  
531 Cretaceous carbonates, and four main strain fields are described, depending on the fault  
532 sets (**Fig. 8**): (1) a compressive stage featured by  $e_y$  with NW-SE trending, similar to  
533 those stage described in Tavani (2012), (2) a normal strain stage with  $e_y$  striking both E-  
534 W and NE-SW (**Fig. 8**, HTM 20, 21, 31 and 32). Finally, a (3) a shear stage (activated  
535 strike-slip faults) and (4) a shear with an extension (strike-slip with normal component)  
536 were described as well. These two late stages are featured by  $e_y$  with NE-SW and NW-  
537 SE trends. The existence of four different strain fields is determined by different ages  
538 during the Cretaceous and different spatial locations in relation to the main structures,



539 the Ubierna Fault System, Hontomin Fault, Cantabrian Thrust, Montorio folded band  
540 and the anticline (**Fig. 8**).

541

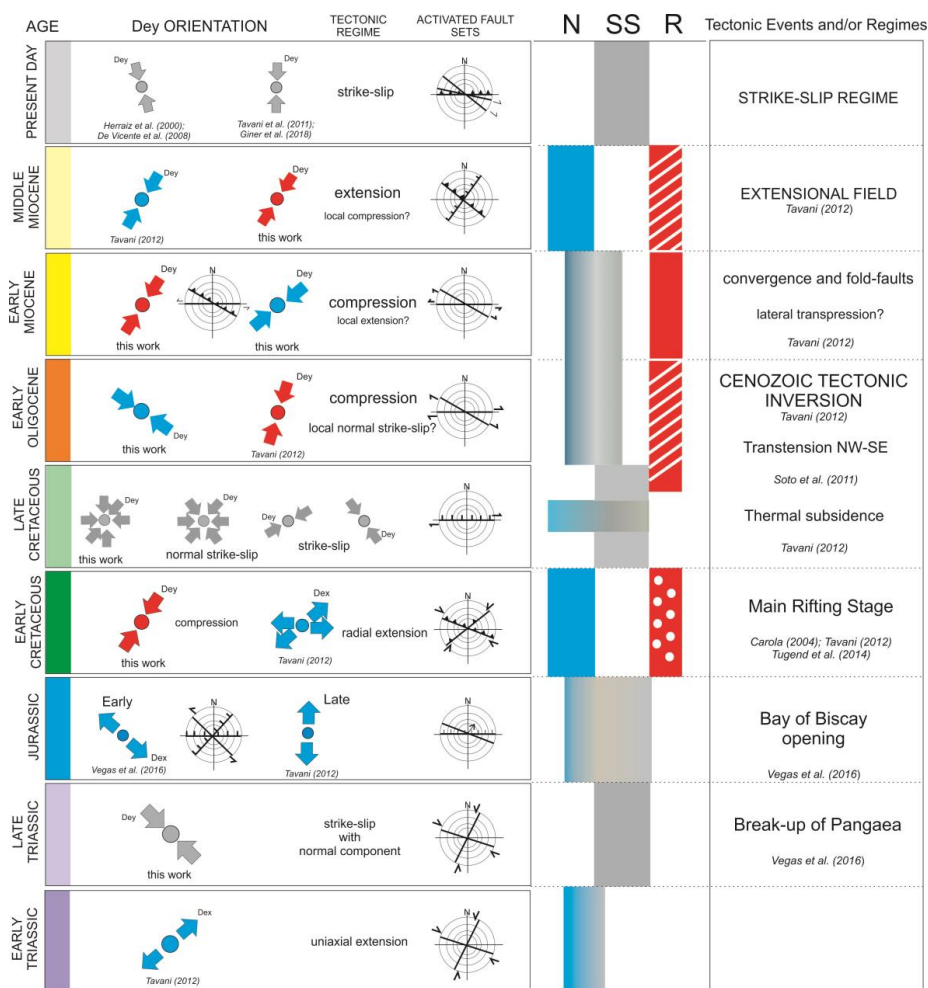
#### 542 *4.4 Cenozoic strain field*

543 The Cenozoic tectonic inversion was widely described in the area by different authors  
544 (e.g. Carola, 2004; Tavani, 2012; Tungend et al., 2014). This tectonic inversion is  
545 related to compressive structures, activating NW-SE and NE-SW thrusts with NW-SE  
546 and NNE-SSW  $e_y$  trends, respectively. The Ubierna Fault has been inverted with a  
547 right-lateral transpressive kinematics during the Cenozoic (Tavani et al., 2011). Early  
548 Oligocene outcrop (HTM13, **Figs. 7c** and **8**) shows an extensional field with  $e_y$  with  
549 NNE-SSW trending. During the Miocene, HTM15 and HTM30 outcrops exhibit the  
550 same  $e_y$  striking, but for compressive tectonic stage (**Figs. 7c** and **8**). In addition, during  
551 the middle Miocene, an extensional tectonic strain is described and characterized by  
552 NNE-SSW and NE-SW trends. Summarizing, the Cenozoic inversion and tectonic  
553 compression are detected during the early middle Miocene, later to the Oligocene, but  
554 during the middle Miocene, only one extensional stage was interpreted.

555 The outcrops located closer to the HPP (HTM 17, 31, 32, **Figs. 5** and **7**), show E-W  
556 faults. HTM05 is located on the Ubierna Fault, showing NW-SE, whilst HTM03 shows  
557 strike-slip NE-SW. Moreover, this station is located within a valley with the same  
558 orientation and surrounding faults have the same orientation (**Fig. 5**). Close to the HPP  
559 facilities, E-W faults are measured. This fault set was activated under a strain field  
560 defined by  $e_y$  with E-W trending and  $K'$ -diagram shows normal faults with strike-slip  
561 component. However, the present-day  $e_y$  with a roughly N-S trend (Herraiz et al., 2000,  
562 Stich et al., 2006), could active E-W faults as reverse faults and hence, more energy



563 would needed to move like seismic sources. In addition, fault dip data obtained from  
 564 structural analysis can be included in geomechanical analysis of fault rupture.  
 565 Strain analysis suggests that the planes that could affect the leakage into the reservoir  
 566 would be those planes parallel to the  $S_{Hmax}$  orientation, that is, NNW-SSE and N-S (**Fig.**  
 567 **7**). Moreover, N50°E  $S_{Hmax}$  orientation could also affect the reservoir. HPP facilities are  
 568 close to WNW-ESE fault although the HTM17 station shows that N-S fault planes  
 569 could play an important role for seepage fluid into the reservoir.



570

571





572 *Figure 9. Tectonic field evolution of the Burgalesa Platform domain (20-km radius circle centered at*  
573 *HPP), interpreted from the paleostrain analysis. The regional tectonic field from other authors are also*  
574 *included. Ages were estimated from the HTM outcrops affecting geological well-dated deposits. N:*  
575 *extensional faulting; R: compressive faulting; SS: strike-slip faulting. Red and white means local*  
576 *paleostrain field, and red with white dots means superposed modern paleostrain field.*

577

## 578 5. DISCUSSION

### 579 5.1. Mesozoic – Cenozoic Paleostrain evolution

580 We propose a tectonic field evolution for the Hontomín CCS area, from the Triassic to  
581 Neogene times (**Fig. 9**), based on the results obtained from the paleostrain analysis (**Fig.**  
582 **8**). Furthermore, the data used in this work were completed from available bibliographic  
583 data of paleostress and paleostrain affecting the Burgalesa Platform (see references in  
584 **Fig. 9**) and large-scale tectonic events.

585 Triassic age is featured by a uniaxial extension determined by a paleostrain field with  $e_x$   
586 striking NE-SW (Tavani, 2012). The oldest tectonic strain field that we have obtained,  
587 recorded during the Late Triassic, is represented by a strike-slip tectonic field with shear  
588 component (**Figs 7a, 8 and 9**), which we have related with the break-up of Pangaea. In  
589 this stage, NE-SW right lateral faults are dominant.

590 No Jurassic outcrops are in the studied area and hence, the Jurassic deformation  
591 assumed in this work comes from Tavani (2012), suggesting the aperture of the Bay of  
592 Biscay in a large-scale N-S extension. Alcalá et al. (2014) pointed out a tectonic  
593 evolution from Lias diparism (Early Jurassic) and N-S tectonic extension, activating E-  
594 W extensional faults. Moreover, Vegas et al. (2016) interpreted a rift extension during  
595 this period.

596 The Early Cretaceous tectonic field shows a  $e_y$  with NE-SW trend, determining a  
597 compressive and convergence local stage (**Figs 7a, 8**). However, we have assumed this



598 strain field as modern, probably during the Cenozoic inversion, overlapping the  
599 extensional regional paleostrain (**Fig. 9**, red with white circles). The Upper Cretaceous  
600 tectonic strain is defined by several  $e_y$  trends, from an initial N-S and NE-SW, to NW-  
601 SE in a final transtensional state, which is in agreement with Soto et al. (2011), being  
602 active even during the Early Oligocene.

603 The tectonic convergence represented by a NE- trending  $S_{Hmax}$ , determining a reverse  
604 field to have taken place during the Early Miocene, although Tavani (2012) pointed out  
605 that the Cenozoic tectonic inversion could start at the Upper Cretaceous. During the  
606 Miocene, normal faults with shear during this period (**Fig. 9**) could be interpreted as  
607 folding fractures. In this case, extensional faulting could appear in the upper part of  
608 anticlines formed by bending. The middle Miocene is interpreted as an extensional stage  
609 with normal strain field.

610 Finally, the active strain field (Miocene-Present-day), shows a local compressional field  
611 with N50°E trending  $e_y$ ,  $S_{Hmax}$  with and the regional field with N150°E trending  $e_y$ ,  
612  $S_{Hmax}$ . The active regional field proposed by Herraiz et al. (2000), Stich et al. (2006),  
613 Tavani et al. (2011) and Alcalde et al. (2014), shows  $e_y$ ,  $S_{Hmax}$  with almost NNW-SSE  
614 and N-S trends.

615

### 616 *5.2 Active faulting in the surrounding of HPP*

617 Quaternary tectonic markers for the UFS are suggested by Tavani et al. (2011).  
618 According to the tectonic behavior of this fault as right-lateral strike-slip, and the fault  
619 segments proposed by Tavani et al. (2011), ranging between 12 and 14 km long, the  
620 question is whether this fault could trigger significant earthquakes and which could be  
621 the maximum associated magnitude. This is a relevant question given that the “natural  
622 seismicity” in the vicinity could affect the integrity of the caprock. Bearing in mind the



623 expectable long-life for the reservoir, estimated in thousands of years, the potential  
624 natural earthquake that this master fault could trigger has to be estimated. In this sense,  
625 it is necessary to depict seismic scenarios related to large earthquake triggering;  
626 however, this type of analysis is beyond the focus of this work.

627 The income information that we have to manage in the area of influence (20 km) is: (a)  
628 the instrumental seismicity, (b) the geometry of the fault, (c) the total surface rupture,  
629 (d) the upper crust thickness and (e) the heat flow across the lithosphere. Starting for the  
630 heat flow value, the Hontomín wells show a value that lies between 62 and 78 mW/m<sup>2</sup>  
631 at a 1,500 m depth approximately (Fernández et al., 1998). Regarding the Moho depth  
632 in the area, these aforementioned authors obtained a value ranging between 36 and 40  
633 km depth, while the lithosphere ranges between 120 and 130 km depth (Torne et al.,  
634 2015). The relevance of this value is the study of the thermal weakness into the  
635 lithosphere that could nucleate earthquakes in intraplate areas (Holford et al., 2011). For  
636 these authors, the comparison between the crustal heat-flow in particular zones, in  
637 contrast with the background regional value, could explain large seismicity and high  
638 rates of small earthquakes occurrence, as the case of the New Madrid seismic zone. For  
639 example, in Australia heat-flow values as much as 90 mW/m<sup>2</sup> are related with  
640 earthquakes  $M > 5$ .

641 Regarding the maximum expected earthquake into the zone, we have applied the  
642 empirical relationships obtained by Wells and Coppersmith (1994). We have used the  
643 equations for strike-slip earthquakes according to the strain field obtained in the area  
644 (pure shear), and the surface rupture segment for the Ubierna Fault System, assuming a  
645 surface rupture segments between 12 and 14 km (Tavani et al., 2011). The obtained  
646 results show that the maximum expected earthquake ranges between M 6.0 and M 6.1.  
647 Wells and Coppersmith (1994) indicate for these fault parameters a total area rupture



648 ranging between 140 and 150 km<sup>2</sup>. Surface fault traces rupture as low as 7 km needs  
649 at least 20 km of depth in order to reach a value of the fault-area rupturing greater than  
650 100 km<sup>2</sup>, in line with a Moho between 36 and 40 in depth.

651 Regarding the instrumental earthquakes recorded into the area, the two largest  
652 earthquakes recorded correspond to magnitude M 3.4 and M 3.3, with a depth ranging  
653 between 8 and 11 km, respectively, and a felt macroseismic intensity of III (EMS98,  
654 [www.ign.es](http://www.ign.es), last access on May, 2019). Both earthquakes occurred between 50 and 60  
655 km of distance from the Hontomín Pilot Plant. Only five earthquakes have been  
656 recorded within the 20-km radius area of influence and with small magnitudes ranging  
657 between M 1.5 and M 2.3. The interesting data is the depth of these earthquakes,  
658 ranging between 10 and 20 km, which suggest that the seismogenic crust could reach 20  
659 km of depth.

660 Furthermore, if E-W sets act as extensional faults in this regional tectonic context, it  
661 would be related to the upper part of the non-deformational compressive zone and reverse  
662 earthquakes would appear with the foci located deeper than 2 km. The strain field is  
663 directly related to the permeability tensor due to rock dissolution. Hence, this value  
664 could play an important role for long-term reservoir expected life.

665

### 666 *5.3 Local tectonic field and Induced Seismicity*

667 The fluid injection into a deep saline aquifer, which is used as CCS, generally increases  
668 the pore pressure. The increasing of the pore pressure migrates from the point of  
669 injection to the whole reservoir. Moreover, changes into the stress field for faults that  
670 are located below the reservoir, could also trigger induced earthquakes (Verdon et al.,  
671 2014). Nevertheless, to understand this possibility and the study the volumetric strain  
672 field spatial distribution is required (Lisle et al., 2009).



673 The injection of 10 k tons of CO<sub>2</sub> in Hontomín (Gastine et al., 2017) represents an  
674 approximate injected volume of CO<sub>2</sub> of 5.5 x10<sup>6</sup> m<sup>3</sup>. The earthquake magnitude to this  
675 fluid-injected volume according to the McGarr (2014) and Verdon et al. (2014) could be  
676 M > 5 if there are faults with a minimum size of 10 km and oriented according to the  
677 present stress field within the influence area (N-S extensional faults and NE-SW/NW-  
678 SE strike slip faults). In the case of HPP, there are faults below the reservoir with this  
679 potential earthquake triggering (Alcalde et al., 2014). On the other hand, overpressure  
680 increasing the permeability of the carbonate reservoir along with the pore pressure  
681 variations of about 0.5 MPa, could trigger earthquakes, as well. Stress-drop related to  
682 fluid injections are also reported (Huang et al., 2016).

683 Le Gallo and de Dios (2018) described two main fault sets affecting the reservoir with  
684 N-S and E-W trend, respectively. According to the present-day stress tensor described  
685 by Herraiz et al. (2000) and Tavani et al. (2011), E-W fault-sets are accommodating  
686 horizontal shortening, which means that the permeability could be low, and N-S faults  
687 could act as strike-slip with trans-tensional component and, hence, higher permeability.  
688 On the other hand, increasing the pore-pressure of E-W faults could reduce de seismic  
689 cycle in these faults. Therefore, special attention has to be paid in microseismicity  
690 related to E-W faults. In this sense, the study of focal mechanisms solutions could  
691 improve the safety management, even for microearthquakes of magnitude lesser than M  
692 3.

693 Moreover, the CO<sub>2</sub> lateral diffusion and pressure variation change during the fluid  
694 injection phase, and then the system would relax before to be increased during the next  
695 injection phase. In this context, the intermittent and episodic injection of CO<sub>2</sub> could also  
696 trigger earthquakes by the stress-field and fluid pressure variations in short time periods.

697



698 6. CONCLUSIONS

699 The application of the analysis for brittle deformation determines the tectonic evolution  
700 of the strain field, applied in Carbon Capture and Sequestration (CCS). The possibility  
701 that pore pressure variations due to fluid injection could change the stress/strain  
702 conditions in the reservoir's caprock, makes the study of the present-day tectonic field  
703 as mandatory for the storage safety operations. In this sense, we have to bear in mind  
704 that this kind of subsurface storage is designed for long-life expectancy, about  
705 thousands of years, and therefore, relevant earthquakes could occur affecting the sealing  
706 and the seepage of CO<sub>2</sub>, compromising the integrity of the reservoir. Hence, we can  
707 conclude from our analysis the following items:

708 (1) The study of this tectonic field allows classifying the geometry of the faults to  
709 prevent prone earthquake-related structures and design monitoring seismic network.

710 (2) The influence area around the facilities of the CCS for studying the active  
711 stress/strain field could reach 20 km from the facility and the tectonic evolution of the  
712 geological history of the reservoir have to be established, adding missing information  
713 from map scale and boreholes. This information could be used from the 3D local  
714 fracture pattern estimation to avoid overpressure for increasing the permeability paths.  
715 Analysis of the stress-drop due to the fluid injection could be combined with this  
716 information to understand potential microseismicity associated with the injection  
717 operations.

718 (3) In the case of Hontomín Pilot-Plant, we have obtained two strain active tectonic  
719 fields featured as shear deformation. These fields are defined by (a) a local tectonic  
720 strain field with  $e_y$ ,  $S_{Hmax}$  striking N50°E and (b) the regional one defined by  $e_y$ ,  $S_{Hmax}$   
721 with N150°E trend. In this context, strike-slip faults with NE-SW trend, reverse faults  
722 with NW-SE trend and reverse oblique faults oriented E-W, are accumulating present-



723 day tectonic deformation. Therefore, we propose the monitoring of E-W faults and the  
724 intersection with strike-slip faults, either due to the possibility to make high-permeable  
725 paths for CO<sub>2</sub> mobility, or due to the possibility to act as compressional faulting due to  
726 the increasing of the pore pressure during injection.

727 (4) Both WNW-ESE fault plus N-S and NE-SW directions are the preferential fault  
728 directions for potential fluid leakage. E-W could act as compressive faults.

729 (5) The Ubierna Fault System represents a tectonically active fault array that could  
730 trigger natural earthquakes as large as M 6 ( $\pm 0.1$ ), from the empirical relationship of the  
731 total rupture segment (ranging between 12 and 14 km, and the total fault-area rupture,  
732 oscillating between 100 and 150 km<sup>2</sup>). Despite the lack of instrumental seismicity into  
733 the influence area, we cannot obviate the potential earthquake occurrence within  
734 intraplate areas due to the long- timescale expected-life of the CCS. The heat-flow  
735 values and thermal crust conditions could determine the presence of intraplate  
736 earthquakes with magnitude  $M > 5$ , for a long timescale (thousands of years).

737 The tectonic evolution and kinematics of the west part of the Burgalesa Platform  
738 domain from upper Triassic to present day show a Cretaceous tectonic inversion, local  
739 reverse strain field during the early Oligocene and early Miocene, with a Normal strain  
740 field during the middle Miocene. The active strain field is now defined by a shear  
741 tectonic defined by  $e_y$  with N-S trend, activating E-W thrust and right-lateral faults with  
742 WNW- and NW- trend.

743 Finally, we state that the determination of the active tectonic strain field, the recognition  
744 and study of active faults within the area of influence (20 km), the estimation of the  
745 maximum potential triggered natural earthquake, the modeling of the stress-change  
746 during the fluid injection and stress-drop, probably improve the operations for a secure  
747 storage. In a short future, earthquake scenarios will be the next step: modeling the



748 Coulomb static stress-changes due to fluid injection and the modeling of intensity maps  
749 of horizontal seismic acceleration.  
750





751 ACKNOWLEDGEMENTS

752 This work has been partially supported by the European Project ENOS: ENabling  
753 Onshore CO<sub>2</sub> Storage in Europe, H2020 Project ID: 653718 and the Spanish project  
754 3GEO, CGL2017-83931-C3-2-P, MICIU-FEDER. The authors would also thank the  
755 crew of CIUDEN at Hontomín facilities for their kind assistance during our fieldwork.  
756



757 REFERENCES

- 758 Alcalde, J., Martí, D., Calahorrano, A., Marzan, I., Ayarza, P., Carbonell, R., Juhlin, C.,  
759 and Pérez-Estaún, A.: Active seismic characterization experiments of the Hontomín  
760 research facility for geological storage of CO<sub>2</sub>, Spain, *Int. J. Greenh. Gas Con.*, 19,  
761 785–795, <http://dx.doi.org/10.1016/j.ijggc.2013.01.039>, 2013.
- 762 Alcalde J., Marzán I., Saura E., Martí D., Ayarza P., Juhlin C., Pérez-Estaún, A., and  
763 Carbonell, R: 3D geological characterization of the Hontomín CO<sub>2</sub> storage site,  
764 Spain: Multidisciplinary approach from seismic, well-log and regional data,  
765 *Tectonophysics*, 627, 6–25, <http://dx.doi.org/10.1016/j.tecto.2014.04.025>, 2014.
- 766 Álvarez-Gómez, J. A.: FMC: a one-liner python program to manage, classify and plot  
767 focal mechanisms, EGU General Assembly, Vienna, Austria, 27 April-02 May,  
768 EGU2014-10887, 2014.
- 769 Anderson, E. M.: *The Dynamics of Faulting and Dyke Formation with application to*  
770 *Britain*, 2<sup>nd</sup> ed., Oliver and Boyd, Edinburgh, 206 pp., 1951.
- 771 Angelier, J.: Determination of the mean principal directions of stresses for a given fault  
772 population, *Tectonophysics*, 56, 17-26, [https://doi.org/10.1016/0040-1951\(79\)90081-](https://doi.org/10.1016/0040-1951(79)90081-7)  
773 [7](https://doi.org/10.1016/0040-1951(79)90081-7), 1979.
- 774 Angelier, J.: Tectonic analysis of fault slip data sets, *J. Geophys. Res.*, 89, 5835-5848,  
775 <https://doi.org/10.1029/JB089iB07p05835>, 1984.
- 776 Angelier, J.: Inversion of field data in fault tectonics to obtain the regional stress-III. A  
777 new rapid direct inversion method by analytical means, *Geophys. J. Int.*, 103, 363-  
778 376, <https://doi.org/10.1111/j.1365-246X.1990.tb01777.x>, 1990.
- 779 Angelier, J. and Mechler, P.: Sur une méthode graphique de recherche des contraintes  
780 principales également utilisable en tectonique et en séismologie: la méthode des  
781 dièdres droits, *B. Soc. Geol. Fr.*, 19, 1309-1318,  
782 <http://dx.doi.org/10.2113/gssgfbull.S7-XIX.6.1309>, 1977.
- 783 Aurell, M., Meléndez, G., Olóriz, F., Bádenas, B., Caracuel, J. E., García-Ramos, J. C.,  
784 Goy, A., Linares, A., Quesada, S. and Robles, S.: Jurassic, in *The geology of Spain*,  
785 pp. 213–253, The Geological Society of London., 2002.
- 786 Bentham, M. and Kirby, G.: CO<sub>2</sub> Storage in Saline Aquifers. *Oil Gas Sci. Technol.*, 60,  
787 559-567, <https://doi.org/10.2516/ogst:2005038>, 2005.
- 788 Bott, M.H.P.: The mechanism of oblique-slip faulting, *Geol. Mag.*, 96: 109-117.  
789 <https://doi.org/10.1017/S0016756800059987>, 1959.



- 790 Capote, R., De Vicente, G., and González Casado, J. M.: An application of the slip  
791 model of brittle deformation to focal mechanism analysis in three different plate  
792 tectonics situation. *Tectonophysics*, 191, 399-409, [https://doi.org/10.1016/0040-](https://doi.org/10.1016/0040-1951(91)90070-9)  
793 [1951\(91\)90070-9](https://doi.org/10.1016/0040-1951(91)90070-9), 1991.
- 794 Calvet, F., Anglada, E. and Salvany, J. M.: El Triásico de los Pirineos, in Vera, J.A.  
795 (ed.) *Geología de España*, pp. 272–274, SGE–IGME, Madrid., 2004.
- 796 Carola, E.: The transition between thin-to-thick-skinned styles of deformation in the  
797 Western Pyrenean Belt. PhD thesis, Universitat de Barcelona, 271 pp., 2004.
- 798 Christensen, N. P.: Report on the current state and need for further research on CO<sub>2</sub>  
799 capture and storage. CO<sub>2</sub>NET, European Carbon Dioxide Network,  
800 [www.co2net.com](http://www.co2net.com), 2004.
- 801 Chu, S.: Carbon Capture and Sequestration, *Science*, 325, 1599,  
802 <http://dx.doi.org/10.1126/science.1181637>, 2009.
- 803 Dallmeyer, R. D. and Martínez-García, E., Eds.: *Pre-Mesozoic Geology of Iberia*,  
804 Springer-Verlag, Berlin Heidelberg, 1990.
- 805 De Vicente, G.: Análisis Poblacional de Fallas. El sector de enlace Sistema Central-  
806 Cordillera Ibérica. Ph.D. thesis, Universidad Complutense de Madrid, Spain, 317 pp.,  
807 1988.
- 808 De Vicente, G., Cloetingh, S., Muñoz-Martín, A., Olaiz, A., Stich, D., Vegas, R.,  
809 Galindo-Zaldivar, J., and Fernández-Lozano, J.: Inversion of moment tensor focal  
810 mechanisms for active stresses around Microcontinent Iberia: Tectonic implications,  
811 *Tectonics*, 27: 1-22, <http://dx.doi.org/10.1029/2006TC002093>, 2008.
- 812 De Vicente, G., Cloetingh, S., Van Wees, J. D., and Cunha, P. P.: Tectonic  
813 classification of Cenozoic Iberian foreland basins, *Tectonophysics*, 502, 38–61,  
814 <http://dx.doi.org/10.1016/j.tecto.2011.02.007>, 2011.
- 815 Etchecopar, A., Vasseur, G., and Daignieres, M.: An inverse problem in microtectonics  
816 for the determination of stress tensor from fault striation analysis, *J. Struct. Geol.*, 3,  
817 51-65, [http://dx.doi.org/10.1016/0191-8141\(81\)90056-0](http://dx.doi.org/10.1016/0191-8141(81)90056-0), 1981.
- 818 Fernández, M., Marzán, I., Correia, A., and Ramalho, E.: Heat flow, heat production,  
819 and lithospheric thermal regime in the Iberian Peninsula, *Tectonophysics*, 291, 29-  
820 53, [http://dx.doi.org/10.1016/S0040-1951\(98\)00029-8](http://dx.doi.org/10.1016/S0040-1951(98)00029-8), 1998.
- 821 Foulger, G. R., Wilson, M., Gluyas, J., Julian, B. R. and Davies, R.: Global review of  
822 human-induced earthquakes, *Earth-Sci. Rev.*, 178, 438–514,  
823 <http://dx.doi.org/10.1016/j.earscirev.2017.07.008>, 2018.



- 824 García-Mondéjar, J., Pujalte, V. and Robles, S.: Características sedimentológicas,  
825 secuenciales y tectoestratigráficas del Triásico de Cantabria y norte de Palencia,  
826 Cuad. Geol. Ibérica, (10), 151–172, 1986.
- 827 García-Mondéjar, J., Agirrezabala, L. M., Aranburu, A., Fernández-Mendiola, P. A.,  
828 Gómez-Pérez, I., López-Horgue, M. and Rosales, I.: Aptian-Albian tectonic pattern  
829 of the Basque-Cantabrian Basin (Northern Spain), *Geological Journal*, 31(1), 13–45,  
830 [http://dx.doi.org/10.1002/\(SICI\)1099-1034\(199603\)31:1<13::AID-GJ689>3.0.CO;2-  
831 Y](http://dx.doi.org/10.1002/(SICI)1099-1034(199603)31:1<13::AID-GJ689>3.0.CO;2-<br/>831 Y), 1996.
- 832 Gastine, M., Berenblyum, R., Czernichowski-lauriol, I., de Dios, J. C., Audigane, P.,  
833 Hladik, V., Poulsen, N., Vercelli, S., Vincent, C., and Wildenborg, T.: Enabling  
834 onshore CO<sub>2</sub> storage in Europe: fostering international cooperation around pilot and  
835 test sites, *Energy Proced.*, 114, 5905–5915,  
836 <http://dx.doi.org/10.1016/j.egypro.2017.03.1728>, 2017.
- 837 Giner-Robles, J.L., Pérez-López, R., Elez, J., Silva, P.G., Rodríguez Escudero, E.,  
838 Canora, C., Rodríguez-Pascua, M.A., Bardají, T., Roquero, E., Huerta, P., Perucha,  
839 M.A.: Strain analysis in the Iberian Peninsula from focal mechanism solutions,  
840 seismic hazard impacts, In: C. Canora, F. Martín, E. Masana, R. Pérez y M. Ortuño,  
841 Eds., pp. 249-252. Tercera reunión ibérica sobre fallas activas y paleosismología,  
842 Alicante (España), 2018.
- 843 Goldberg, D. S., Kent, D. V., and Olsen, P. E.: Potential on-shore and off-shore  
844 reservoirs for CO<sub>2</sub> sequestration in Central Atlantic magmatic province basalts, *P.*  
845 *Natl. Acad. Sci. USA*, 107, 1327–1332, <http://dx.doi.org/10.1073/pnas.0913721107>,  
846 2010.
- 847 Gómez, M., Vergés, J. and Riaza, C.: Inversion tectonics of the northern margin of the  
848 Basque Cantabrian Basin, *Bulletin de la Société Géologique de France*, 173(5), 449–  
849 459, <http://dx.doi.org/10.2113/173.5.449>, 2002.
- 850 Herraiz, M., De Vicente, G., Lindo-Naupari, R., Giner, J., Simón, J.L., González-  
851 Casado, J.M., Vadillo, O., Rodríguez-Pascua, M.A., Cicuéndez, J.I., Casas, A.,  
852 Cabañas, L., Rincón, P., Cortés, A.L., Ramírez, M., and Lucini, M.: The recent  
853 (upper Miocene to Quaternary) and present tectonic stress distributions in the Iberian  
854 Peninsula, *Tectonics*, 19, 762–786, <https://doi.org/10.1029/2000TC900006>, 2000.
- 855 Holford, S. M., Hillis, R. R., Hand, M., and Sandiford, M.: Thermal weakening  
856 localizes intraplate deformation along the southern Australian continental margin,



- 857 Earth Planet. Sc. Lett., 305, 207–214, <http://dx.doi.org/10.1016/j.epsl.2011.02.056>,  
858 2011.
- 859 Huang, Y., Beroza, G. C., and Ellsworth, W. L.: Stress drop estimates of potentially  
860 induced earthquakes in the Guy-Greenbrier sequence, *J. Geophys. Res.-Sol. Ea.*, 121,  
861 6597–6607, <http://dx.doi.org/10.1002/2016JB013067>, 2016.
- 862 Kaverina, A. N., Lander, A. V., and Prozorov, A. G.: Global creepex distribution and its  
863 relation to earthquake-source geometry and tectonic origin, *Geophys. J. Int.*, 125,  
864 249-265, <https://doi.org/10.1111/j.1365-246X.1996.tb06549.x>, 1996.
- 865 Le Gallo, Y. and de Dios, J. C.: Geological Model of a Storage Complex for a CO<sub>2</sub>  
866 Storage Operation in a Naturally-Fractured Carbonate Formation, *Geosciences*, 2018,  
867 8, 354, <http://dx.doi.org/10.3390/geosciences8090354>, 2018.
- 868 Le Pichon, X. and Sibuet, J.-C.: Western extension of boundary between European and  
869 Iberian plates during the Pyrenean orogeny, *Earth and Planetary Science Letters*,  
870 12(1), 83–88, [http://dx.doi.org/10.1016/0012-821X\(71\)90058-6](http://dx.doi.org/10.1016/0012-821X(71)90058-6), 1971.
- 871 Lepvrier, C. and Martínez-García, E.: Fault development and stress evolution of the  
872 post-Hercynian Asturian Basin (Asturias and Cantabria, northwestern Spain),  
873 *Tectonophysics*, 184, 345, [http://dx.doi.org/10.1016/0040-1951\(90\)90447-G](http://dx.doi.org/10.1016/0040-1951(90)90447-G), 1990.
- 874 Lisle, R. J., Aller, J., Bastida, F., Bobillo-Ares, N. C., and Toimil, N. C.: Volumetric  
875 strains in neutral surface folding, *Terra Nova*, 21, 14–20,  
876 <http://dx.doi.org/10.1111/j.1365-3121.2008.00846.x>, 2009.
- 877 McGarr, A.: Maximum magnitude earthquakes induced by fluid injection, *J. Geophys.*  
878 *Res.*, 119, 1008–1019, <https://doi.org/10.1002/2013JB010597>, 2014.
- 879 McNamara, D.D. Methods and techniques employed to monitor induced seismicity  
880 from carbon capture and storage, *GNS Science Report 2015/18*, 23 pp.,  
881 <http://dx.doi.org/10.13140/RG.2.2.13830.98888>, 2016.
- 882 Muñoz, J. A.: Evolution of a continental collision belt: ECORS-Pyrenees crustal  
883 balanced cross-section, in *Thrust Tectonics*, edited by K. R. McClay, pp. 235–246,  
884 Springer Netherlands, Dordrecht., 1992.
- 885 Ogaya, X., Ledo J., Queralt P., Marcuello, A., and Quintà, A.: First geoelectrical image  
886 of the subsurface of the Hontomín site (Spain) for CO<sub>2</sub> geological storage: A  
887 magnetotelluric 2D characterization, *Int. J. Greenh. Gas Con.*, 13, 168–179,  
888 <https://doi.org/10.1016/j.ijggc.2012.12.023>, 2013.
- 889 Orr, F.M.: Onshore Geologic Storage of CO<sub>2</sub>, *Science*, 325, 1656-1658,  
890 <http://dx.doi.org/10.1126/science.1175677>, 2009.



- 891 Pérez-López, R., Mediato, J.F., Rodríguez-Pascua, M.A., Giner-Robles, J.L., Martínez-  
892 Orío, R., Arenillas-González, A., Fernández-Canteli, P., de Dios, J.C., Loubeau, L.:  
893 Aplicación del análisis estructural y campos de deformación para el estudio de  
894 sismicidad inducida en almacenamiento profundo: Hontomín, In: C. Canora, F.  
895 Martín, E. Masana, R. Pérez y M. Ortuño, Eds., pp. 279-282. Tercera reunión ibérica  
896 sobre fallas activas y paleosismología, Alicante (España), 2018.
- 897 Pearce, J. M.: What can we learn from Natural Analogues? An overview of how  
898 analogues can benefit the geological storage of CO<sub>2</sub>, in: Advances in the Geological  
899 Storage of Carbon Dioxide, edited by: Lombardi, S., Altunina, L. K., and Beaubien,  
900 S. E., Springer, Dordrecht, The Netherlands, 129–139, 2005.
- 901 Pegoraro, O.: Application de la microtectonique à un étude de neotectonique. Le golfe  
902 Maliaque (Grèce centrale). Ph.D. thesis, U.S.T.L. Montpellier, France, 41 pp., 1972.
- 903 Permentier, K., Vercammen, S., Soetaert, S., and Schellemans, Ch.: Carbon dioxide  
904 poisoning: a literature review of an often forgotten cause of intoxication in the  
905 emergency department, International Journal of Emergency Medicine, 10, 14,  
906 <http://dx.doi.org/10.1186/s12245-017-0142-y>, 2017.
- 907 Quintà, A. and Tavani S., The foreland deformation in the south-western Basque–  
908 Cantabrian Belt (Spain), *Tectonophysics*, 576–577, 4–19,  
909 <http://dx.doi.org/10.1016/j.tecto.2012.02.015>, 2012.
- 910 Reches, Z.: Faulting of rocks in three-dimensional strain fields, II. Theoretical analysis,  
911 *Tectonophysics*, 95, 133-156, [https://doi.org/10.1016/0040-1951\(83\)90264-0](https://doi.org/10.1016/0040-1951(83)90264-0), 1983.
- 912 Reches, Z.: Determination of the tectonic stress tensor from slip along faults that obey  
913 the Coulomb yield condition, *Tectonics*, 7, 849-861,  
914 <https://doi.org/10.1029/TC006i006p00849>, 1987.
- 915 Rice, S. A.: Health effects of acute and prolonged CO<sub>2</sub> exposure in normal and sensitive  
916 populations, Second Annual Conference on Carbon Sequestration, Alexandria,  
917 Virginia, USA, 5-6 May, 2003.
- 918 Roca, E., Muñoz, J. A., Ferrer, O. and Ellouz, N.: The role of the Bay of Biscay  
919 Mesozoic extensional structure in the configuration of the Pyrenean orogen:  
920 Constraints from the MARCONI deep seismic reflection survey, *Tectonics*, 30(2),  
921 <https://10.1029/2010TC002735>, 2011.
- 922 Röhmann, L., Tillner, E., Magri, F., Kühn, M., and Kempka, T.: Fault reactivation and  
923 ground surface uplift assessment at a prospective German CO<sub>2</sub> storage site, *Energy*  
924 *Proced.*, 40, 437–446. <http://dx.doi.org/10.1016/j.egypro.2013.08.050>, 2013.



- 925 Serrano, A. and Martínez del Olmo, W.: Tectónica salina en el Dominio Cantabro–  
926 Navarro: evolución, edad y origen de las estructuras salinas, in: Formaciones  
927 evaporíticas de la Cuenca del Ebro y cadenas periféricas, y de la zona de Levante,  
928 edited by: Orti, F. and Salvany, J.M., Empresa Nacional De Residuos Radiactivos  
929 S.A, ENRESA-GPPG, Barcelona, Spain, 39–53, 1990.
- 930 Simpson, R. S.: Quantifying Anderson's fault types, *J. Geophys. Res.*, 102, 17,909–  
931 17,919, <https://doi.org/10.1029/97JB01274>, 1997.
- 932 Stich, D., Serpelloni, E., Mancilla, F. L., and Morales, J.: Kinematics of the Iberia–  
933 Maghreb plate contact from seismic moment tensors and GPS observations,  
934 *Tectonophysics*, 426, 295–317. <https://doi.org/10.1016/j.tecto.2006.08.004>, 2006.
- 935 Soto R., Casa-Sainz A. M., and Villalaín, J. J.: Widespread Cretaceous inversion event  
936 in northern Spain: evidence from subsurface and palaeomagnetic data, *Journal of the*  
937 *Geological Society London*, 168, 899–912, [http://dx.doi.org/10.1144/0016-](http://dx.doi.org/10.1144/0016-76492010-072)  
938 [76492010-072](http://dx.doi.org/10.1144/0016-76492010-072), 2011.
- 939 Tavani, S., Quintá, A., and Granado, P.: Cenozoic right-lateral wrench tectonics in the  
940 Western Pyrenees (Spain): The Ubierna Fault System, *Tectonophysics*, 509, 238–  
941 253, <http://dx.doi.org/10.1016/j.tecto.2011.06.013>, 2011.
- 942 Tavani, S.: Plate kinematics in the Cantabrian domain of the Pyrenean orogeny, *Solid*  
943 *Earth*, 3, 265–292, <http://dx.doi.org/10.5194/se-3-265-2012>, 2012
- 944 Tavani, S., Carola, C., Granado, P., Quintà, A., and Muñoz, J. A.: Transpressive  
945 inversion of a Mesozoic extensional forced fold system with an intermediate  
946 décollement level in the Basque - Cantabrian Basin (Spain), *Tectonics*, 32,  
947 <http://dx.doi.org/10.1002/tect.20019>, 2013.
- 948 Torne, M., Fernández, M., Vergés, J., Ayala, C., Salas, M. C., Jimenez-Munt, I.,  
949 Buffett, G. G., and Díaz, J.: Crust and mantle lithospheric structure of the Iberian  
950 Peninsula deduced from potential field modeling and thermal analysis,  
951 *Tectonophysics*, 663, 419–433, <http://dx.doi.org/10.1016/j.tecto.2015.06.003>, 2015.
- 952 Tugend, J., Manatschal, G., Kuszniir, N. J., Masini, E., Mohn, G. and Thion, I.:  
953 Formation and deformation of hyperextended rift systems: Insights from rift domain  
954 mapping in the Bay of Biscay-Pyrenees, *Tectonics*, 33(7), 1239–1276,  
955 <http://dx.doi.org/10.1002/2014TC003529>, 2014.
- 956 Vegas, R., Vázquez, J. T., Olaiz, A. J., and Medialdea, T.: Tectonic model for the latest  
957 Triassic - Early Jurassic extensional event in and around the Iberian Peninsula,  
958 *Geogaceta*, 60, 23–26, 2016.



- 959 Verdon, J. P.: Significance for secure CO<sub>2</sub> storage of earthquakes induced by fluid  
960 injection, *Environ. Res. Lett.*, 9, 064022 (10pp), [http://dx.doi.org/10.1088/1748-](http://dx.doi.org/10.1088/1748-9326/9/6/064022)  
961 [9326/9/6/064022](http://dx.doi.org/10.1088/1748-9326/9/6/064022), 2014.
- 962 Verdon, J. P., Stork, A. L., Bissell, R. C., Bond, C. E., and Werner, M. J.: Simulation of  
963 seismic events induced by CO<sub>2</sub> injection at In Salah, Algeria, *Earth Planet. Sci. Lett.*,  
964 426, 118–129, <http://dx.doi.org/10.1016/j.epsl.2015.06.029>, 2015.
- 965 Vergés, J., Fernández, M. and Martínez, A.: The Pyrenean orogen: pre-, syn-, and post-  
966 collisional evolution, *J. Virt. Ex.*, 08, <http://dx.doi.org/10.3809/jvirtex.2002.00058>,  
967 2002.
- 968 Wells, D. L. and Coppersmith, K. J.: New empirical relationships among magnitude,  
969 rupture length, rupture width, rupture area, and surface displacement, *B. Seismol.*  
970 *Soc. Am.*, 84, 974–1002, 1994.
- 971 Wilson, M. P., Foulger, G. R., Gluyas, J. G., Davies, R. J., and Julian, B. R.: HiQuake  
972 the human-induced earthquake database, *Seismol. Res. Lett.*, 88, 1560-1565,  
973 <http://dx.doi.org/10.1785/0220170112>, 2017.
- 974 Winthaegen, P., Arts, R., and Schroot, B.: Monitoring Subsurface CO<sub>2</sub> Storage. *Oil Gas*  
975 *Sci. Technol.*, 60, 573-582, 2005.
- 976 Žalohar, J. and Vrabec, M.: Combined kinematic and paleostress analysis of fault-slip  
977 data: The Multiple-slip method, *J. Struct. Geol.*, 30, 1603–1613,  
978 <http://dx.doi.org/10.1016/j.jsg.2008.09.004>, 2008.